Doctoral Thesis

Design of Functional Separator Membrane for the Advanced Energy Storage Devices

Myoungsoo Shin

Department of Energy Engineering

(Energy Engineering)

Graduate School of UNIST

2019

Design of Functional Separator Membrane for the Advanced Energy Storage Devices

Myoungsoo Shin

Department of Energy Engineering
(Energy Engineering)

Graduate School of UNIST

Design of Functional Separator Membrane for the Advanced Energy Storage Devices

A thesis/dissertation
submitted to the Graduate School of UNIST
in partial fulfillment of the
requirements for the degree of
Doctor of Philosophy

Myoungsoo Shin

06/14/2019
Approved by

_____

Advisor
Nam-Soon Choi

Design of Functional Separator Membrane for the Advanced Energy Storage Devices

Myoungsoo Shin

This certifies that the thesis/dissertation of Myoungsoo Shin is approved.

06/14/2019

Signature

_____

Advisor: Nam-Soon Choi

signature

_____

Prof. Sang-Young Lee

signature

_____

Prof. Soojin Park

signature

_____

Prof. So Youn Kim

signature

_____

Prof. Seungmin Yoo

Abstract

Porous materials have been received great interest in many applications for filtration, separator membrane, catalyst support, and template for nanostructured materials owing to their various advantages such as high surface area and unique structure. In the energy storage device fields, especially Li-ion batteries (LIBs), the porous materials have been widely used as active materials, binders, separator membranes, and current collector. Among them, the separator membrane is an important component in determining battery performances. To date, numerous researches have been carried out to develop advanced separator membrane with multifunctionality, cost-effectiveness, and easy processability. Depending on their purposes, the porous separator membranes have been prepared via various fabrication techniques. Among them, a non-solvent induced phase separation (NIPS) represents one of the most promising fabrication methods for the separator membranes of energy-storage devices owing to its a scalable fabrication, low cost, morphology tailored for various requirements, and a wide selection of materials.

In this thesis, we propose the design of phase separation behavior between polymers and solvents in thermodynamic and kinetic aspects for fabricating multitalented separator membrane via NIPS. We induced the different phase separation behavior by adjusting the affinity between solvent and nonsolvent. In addition, we also modify the surface energy and molecular weight of the polymer, leading to the fabrication of different porous structure after phase inversion. Therefore, we can control the mechanical properties of the separator membrane with unique characteristics and its original polymeric properties. Using the proposed multitalented separator membranes, we fabricate the fully stretchable aqueous rechargeable lithium-ion batteries (ARLBs), and high-performance LIBs comprising Mn-based cathode materials at a practical loading density under high-temperature operation.

In chapter I, we briefly introduce the research background of NIPS technique and its main parameters which determines the porous structure. Furthermore, we discuss the recent porous membranes by using phase inversion methods for energy storage applications.

In chapter II, we present SBS block copolymer based highly stretchable separator membrane by NIPS method (SBN separator membrane) by tuning the affinity between solvent and nonsolvent. This is the first demonstration of reliable stretchable separator membrane using NIPS method which has the advantage of scalable fabrication. Moreover, tuning the main parameter of NIPS, we prepared the suitable porous structure and stretchability to be compatible with deformable energy-storage devices. The SBN separator membrane exhibits a high stretchability of around 270% strain and porous structure with a porosity of 61%. Using the SBN separator membrane, we have demonstrated reliable stretchable separator which compatible with both organic and

aqueous electrolyte based deformable energy-storage devices with stable cycle retention performances under a stretching condition of 100%. This study presents a unique strategy for designing stretchable separator for a variety of applications.

In chapter III, we employed (3-glycidoxypropyl) trimethoxysilane (GPTMS) as a surface modifier enabling the seaweed-extracted material, agar, to exhibit different phase separation behavior during the nonsolvent-induced phase separation (NIPS) process, which eventually lead to the outstanding separator membrane with features of a well-defined porous structure, superior mechanical robustness, high ionic conductivity, and good thermal stability. Here, we demonstrated that GPTMS-modified Agar (G-Agar) separator membrane coupled with a pure Agar binder to the $LiNi_{0.5}Mn_{1.5}O_4$//graphite full cell exhibits exceptional improvement in electrochemical performance under the elevated temperatures (55°C) due to abilities of Mn^{2+} chelation and PF_5 stabilization, as compared to a commercial cell with the typical binder and polyolefin-based separator membrane. This study proposes that Agar's multifunctionalities, along with cost-effectiveness, make it feasible for wide applications in energy storage device fields and offers a class of multifunctional natural material for high-performance LIBs.

Contents

List of figures

[Chapter 1]

[Chapter 2]

density (1 C/1 C). d) Nyquist plots (impedance spectra) of the half cell with PE, agar, and 0.5G-Agar separator membranes after 100 cycles at 60 . e) TOF-SIMS analysis of the separator membranes after immersion in a water-contained electrolyte.

Figure 3-5. Electrochemical performances of LNMO/graphite full cell with PE, agar, and 0.5G-Agar separator membrane. a) Schematic illustration of the LNMO/graphite full cell configuration. b) Galvanostatic charge-discharge curves of full cells with different separators and binder at a rate of 0.1 C. c) Cycling performances at a charge/discharge rate (1 C/1 C) under different temperatures. d) Elevated temperature (55) storage ability of the full cell with PE, agar, and 0.5G-Agar separator membrane. e) Capacity retention (%) of the LMO or LNMO full cells as a function of areal energy density under high temperature.[18,22,44-47]

Table S3-1. Peak assignment of FT-IR spectra of agar and G-Agar separator.

Table S3-2. Fitting results for the impedance spectra in Figure 4e.

Figure S3-1. FT-IR analysis of agar and G-Agar separator membrane.

Figure S3-2. Digital photographs of large-scale G-Agar film fabrication process.

Figure S3-3. Digital photographs of agar and G-Agar solutions with various GPTMS modification.

Figure S3-4. Contact angle of agar and G-Agar separator to the electrolyte (1 M LiPF6 in EC/DEC (1/1 v/v)).

Figure S3-5. SEM images of PE, agar and G-Agar separator before and after thermal treatment.

Figure S3-6. Digital photographs of PE, agar and G-Agar separator before and after thermal treatment.

Figure S3-7. Cyclic voltammetry (CV) characterization of 0.5G-Agar separator membrane.

Figure S3-8. ICP-MS results of PE, agar, 0.5G-Agar separator membrane after immersing Mn2+ ion contained electrolyte (10mM Mn(ClO4)2-contained 1M LiPF6 in EC/DEC 1/1 v/v).

Figure S3-9. a) SEM and b) EDX results of PE, agar, and G-Agar separator after 100 cycles at high temperature.

Figure S3-10. Overpotential of PE, agar and G-Agar with LNMO/graphite full cell at first cycle.

Figure S3-11. Frist cycle of the LNMO/graphite full cell with high loading density (1.9 mA h cm-2) with different separator and binder at a rate of 0.1 C under 25 .

Figure S3-12. a) Cycle performance and b) CE resultof LNMO/graphite full cell with high loading energy density (1.9 mA h cm-2) at a rate of 1 C under 60 .

Nomenclature

LIB	Lithium ion battery
NIPS	Nonsolvent induced phase separation
ARLBs	Aqueous rechargeable lithium-ion batteries
SBS	poly(styrene-*b*-butadiene-*b*-styrene) polymer
Mn	Manganese
SEM	scanning electron microscopy
XRD	X-ray diffraction
SBN	SBS block copolymer based highly stretchable separator membrane by NIPS
PC	polycarbonate
Li_2SO_4	Lithium sulfate
NMP	N-methyl Pyrrolinone
GPTMS	(3-glycidoxypropyl) trimethoxysilane
EC	ethylene carbonate
EDX	energy-dispersive X-ray spectroscopy
EIS	electrochemical impedance spectroscopy
CV	cyclic voltammetry
LNMO	Lithium nickel manganese spinel
G-Agar	GPTMS modified agar
PE	polyethylene
EIS	electrochemical impedance spectroscopy
GF	glass fiber
FT-IR	Fourier transform infrared
GPE	gel polymer electrolytes
LMO	lithium manganese oxide
TOF-SIMS	Time-of-flight secondary ion mass spectrometry
THF	Tetrahydrofuran
ICE	initial coulombic efficiency
PI	poly imide
LFP	lithium iron phosphate
LEDs	light emitting diodes
CB	carbon black
$LiPF_6$	lithium hexafluorophosphate

CNT	carbon nanotube
LTO	Lithium titanate
PDMS	Poly(dimethylsiloxane)
SD	Spinodal decomposition
NG	Nucleation and growth
TIPS	Thermally induced phase separation
VIPS	Vapor induced phase separation
SIPS	Solvent evaporation-induced phase separation
TPE	Thermoplastic elastomer
Ar	Argon
AC	Activated carbon
Al	Aluminum
Cu	Copper
3D	Three-dimensional
HSP	Hansen solubility parameter
O_2	Oxygen
Ni	Nickel
Zn	Zinc
HF	hydrofluoric acid
USD	United States dollar
Gr	graphite
DMF	Dimethylformamide
DMC	dimethyl carbonate
F	fluorine
PO_2F_2	Difluorophosphate
PVDF	Polyvinylidene fluoride
Li	Lithium
SBR	styrene-butadiene rubber
CMC	carboxyl methylcellulose
FEC	Fluoroethylene carbonate
EMC	Ethylmethyl carbonate
PFE	partially fluorinated ether based on a mixture of 1,1,1,2,2,3,3,4,4-nonafluoro-4-methoxybutane and 2-(difluoro(methoxy)methyl)-1,1,1,2,3,3,3-heptafluoropropane
CaH_2	calcium hydride

DEC	diethyl carbonate
PF_5	Phosphorus pentafluoride
R_s	electrolyte resistance
R_{SEI}	impedance associated with the interfacial layer on anode electrodes
R_{ct}	resistance for the faradaic charge transfer reaction
Z_W	Warburg diffusional impedance
LiF	Lithium fluoride
OCV	Open-circuit voltage
ΔG_m	Gibbs free energy of mixing
PAN	Polyacrylonitrile
PMMA	poly(methyl methacrylate)
PVDF-co-HFP	poly(vinylidene fluoride-co-hexafluoropropylene)
PPO	poly(phenylene oxide)
PVA	poly(vinyl alcohol)
LiF	Lithium fluoride

1. Introduction

1.1 Background

In recent years, the concerns about ever-growing energy consumptions have amplified the demands for next-generation storage devices. Especially, lithium-ion batteries (LIBs) have been effectively utilized in the variety of portable electronic devices such as cellular phones, laptops, tablets, cameras, and bluetooth headsets owing to their design flexibility, no memory effect, high energy density, and long cycle life.[1-3] As the usage of LIBs continuous to increase, many researchers are seeking to develop an advanced battery with cheap, eco-friendly, higher energy density, and flexibility.[4-6] The typical approach to improve the LIBs performance is to optimize their main components. Conventional LIBs consist of electrodes (cathode and anode), electrolytes ($LIPF_6$-based organic electrolytes) and a polyolefin-based separator membrane. [7] Among them, the separator membrane plays an important role in separating between the cathode and anode to avoid the short circuit, while offering the ion-conducting pathway to complete the circuit.[8] Depending on their applications, the separator membranes have been made through various preparation techniques such as stretching, electrospinning, and phase inversion for the desired porous morphology.[9] Especially, the phase inversion methods have been used for preparing porous polymeric films in various fields.[10] However, a co-diffusion of solvent and nonsolvent during phase inversion usually makes fingerlike voids in the membrane, which is unsuitable to use for energy storage devices due to low mechanical properties, and unequal ion transfer through separator membrane. Moreover, the optimization of preparation conditions to develop a uniformly porous structure is difficult because various factors affect the final membrane structure.[11]

In the 1960s, the Loeb and Sourirajan developed the asymmetric membranes, which is a breakthrough in membrane technology.[12] In their study, the phase inversion technique was introduced to transform a liquid polymer solution into a solid polymeric porous film. Over the last half-century, excessive knowledge has been created about phase inversion membranes formed by immersion precipitation, also known as nonsolvent induced phase inversion (NIPS). The immersion precipitation is early to be commercially utilized and is one of the most widespread membrane formation technique because it allows for preparation of the various membrane morphologies via a simple step.[11]

To date, porous membranes fabricated by NIPS have been widely used in various fields

including gas separations[13], reverse osmosis membrane,[14] and energy-storage devices (specially LIBs[15]) owing to its scalability, morphology tailored for individual applications, and a wide selection of polymeric material. Furthermore, there has been growing interest in the fabrication of separator membrane for LIBs via NIPS because it can control the porous morphology by tuning several key parameters for tailoring porosity and mechanical properties of the separator membranes.[15~18]

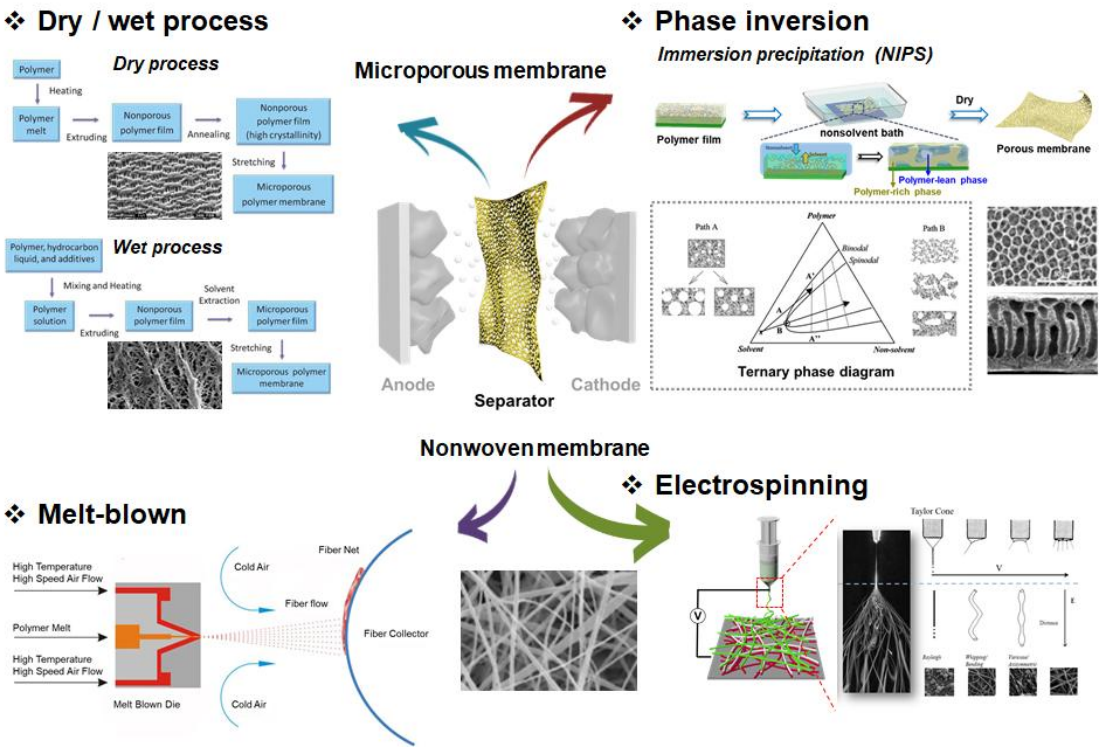

Figure 1-1. Various synthetic methods of separator membrane.

1.2 Nonsolvent induced phase separation

To date, the phase inversion method has been widely used for the preparation of porous membrane in secondary battery fields, especially in LIBs. The separator membrane that meets numerous requirements of LIBs can be easily obtained via phase inversion methods. In the phase inversion method, the thermodynamic equilibrium of a homogeneous polymeric solution with a certain composition is broken up in some physical ways (demixing). After then, the solution change from single phase into two phases consisting of polymer-rich and polymer-lean phases, resulting in the membrane matrix and pores, respectively.[19]

The thermodynamic state of the polymer solution can be explained by a phase diagram (Figure 1-2). In this diagram, there are a homogeneous one-phase region and unstable two-phase region divided by a binodal line which is estimated based on the Flory-Huggins thermodynamics or by measuring the cloud point.[20] The spinodal line is determined by the derivatives of the binodal curve. When the composition of the polymer solution is in the unstable region, the polymer phase is separated by a spinodal decomposition (SD) mechanism and leads to bi-continuous structured liquid-liquid separation. As a result, a bi-continuous porous structure is formed in the end. On the contrary, when the composition of the polymer solution is in the meta-sable region, the polymer phase is separated by a nucleation and growth (NG) mechanism and leads to the formation of closed and cellular pore in the end. An important point of the phase separation is the variation in the thermodynamic state of the polymer solution. Thus, there are wet or dry phase separation process such as thermally induced phase separation (TIPS), vapor induced phase separation (VIPS), solvent evaporation-induced phase separation (SIPS), and nonsolvent induced phase separation (NIPS) according to the different physical ways of changing the thermodynamic states of the polymer solution (Figure 1-3). Among the porous membrane preparation techniques, the immersion precipitation (e.g., NIPS) is one of the most promising fabrication methods for the separator membranes of energy-storage devices (specially LIBs) due to its a scalable preparation, morphology tailored for various applications, and a wide selectable of polymer materials.

In the NIPS method, the break of thermodynamic equilibrium is induced by immersing one-phase polymer film into the nonsolvent bath (coagulation bath) as illustrated in Figure1-4.[11,19] The porous morphology is typically determined by the thermodynamic states of the polymer chain in the nonsolvent bath. At this moment, there are three main factors (e.g, polymer, solvent, and nonsolvent) determining the thermodynamic and kinetics of the polymer. In the early, Strathmann et al. explained the thermodynamic behavior of polymer by using ternary phase diagram as illustrated in Figure 1-5.[10] Each corner of the triangle means the main parameter (polymer,

solvent, and nonsolvent), and the binodal line divides the solution phase into one-phase region and two-phase region. The position of the binodal line is fixed by interactions between three main parameters. Any point in the ternary diagram means a composition of three factors. The one-phase region is miscible, while the two-phase region is separated into polymer-rich and polymer-lean phases. In the two-phase region, the composition of three component of the polymer-rich phase and polymer-poor phase is determined by tie line, which connects a pair of equilibrium of the binodal line.

A homogeneous one phase polymer solution starts to change upon immersing in the nonsolvent bath. The pore forming mechanism of NIPS can be divided into instantaneous demixing and delayed demixing, depending on the solvent–nonsolvent exchange rate. In the short time ($t < 1$ s) after immersing, the exchange between solvent and nonsolvent starts to under the driving force caused by the gradient in chemical potential. When the composition path penetrates into the binodal line quickly, the instantaneous liquid-liquid demixing occurs (black line), leading to the fast precipitation of the polymer in the nonsolvent bath and eventually developing a large "finger-like" macrovoids structure. On the contrary, the delayed liquid-liquid demixing (red line) has only single-phase region upon immersion. After a period of time, polymer composition begins to cross the binodal line (demixing), leading to the slow precipitation of the polymer in the nonsolvent bath and forming a spherical-type "sponge-like" pore structure as illustrated in Figure 1-6.[19] These two types of pore structures have a major impact on the application of the membrane. In the LIBs separator application, especially, the large macrovoids help to accelerate the rapid transfer of Li-ion between anode and cathode electrode. However, they easily cause the self-discharging and internal short-circuit problem due to leakage current between the electrode; furthermore, lithium dendrite can contact to the counter electrode through macrovoid, which are the primitive reasons of cell explosions or fires. Lastly, the separator membrane with macrovoids exhibits low mechanical property, and it is limited to apply to a deformable energy storage device such as flexible and stretchable batteries.[21] Therefore, the choice of the solvent-nonsolvent pair is the most important factor in the NIPS system because the affinity between solvent and nonsolvent primarily determines the demixing rate. Generally, when the mutual affinity is high, instantaneous demixing occurs and a more porous membrane is formed. In the case of low affinity with each other, the nonporous separator membrane will be obtained.[22]

Flory and Huggins developed a two-dimensional lattice-based model to deal with the thermodynamics of polymer solution.[23] In this model, solvent molecules and polymer segments are supposed to be the same size, and only one polymer segment or molecule can fill a single lattice site. In the ternary component system, the Gibbs free energy of mixing (ΔG_m) is calculated

such as the following equation:

$$\Delta G_m/RT = (n_1 ln\emptyset_1 + \ n_2 ln\emptyset_2 + n_3 ln\emptyset_3 + \ \chi_{12} n_1\emptyset_2 + \chi_{13} n_1\emptyset_3 + \chi_{23} n_2\emptyset_3)$$

where T is absolute temperature, R is gas constant, n_1 and n_2 are the numbers of solvents (component 1), nonsolvent (component 2), and polymer (component 3) molecules, respectively. $\emptyset$ is the volume fraction and χ_{12} is the interaction parameter between component 1 and 2. The interaction parameter can be estimate by solubility parameter (δ), which help choose appropriate solvent-nonsolvent pair.

The Flory interaction parameter can be approximated from solvent (δ1) and nonsolvent (δ2) solubility parameters using the following relation:

$$\chi_{12} = \ \frac{v_1}{RT}(\delta_1 - \delta_2)^2$$

where R is the ideal gas constant and v_1 is the molar volume of component 1.

Hansen proposed the solubility parameter related to the total cohesive energy comprising the dispersion forces (δ_d), permanent dipole-permanent dipole forces (δ_p), and hydrogen bonding (δ_h).[24] The solubility parameter is equal to

$$\delta = \sqrt{\delta_d^2 + \delta_p^2 + \delta_h^2}$$

Determination of solvent δ_d and δ_p is described by Prausnitz and Blanks. [r25] Beerbower and Hansen calculated the solvent δ_p such as

$$\delta_p = 37.4\frac{\mu}{V^{0.5}}$$

where μ is the dipole moment of solvent and V is the molar volume of the solvent. The δ_h has been determined by subtracting δ_d and δ_p from δ. Using the above equations, the solubility parameter values of various solvent could be calculated as Table 1. In addition, by comparing the solubility parameter of various solvents, the affinity between solvent and nonsolvent can be predicted by using a hansen solubility parameter distance (R_{HSP}), which was developed by Skaarup.[26] The distance between solvent (1) and nonsolvent (2) meaning their affinities based on their specific Hansen solubility parameters could be calculated by using the following equation

$$R_{HSP} = \ \sqrt{4(\delta_{d2} - \delta_{d1})^2 + (\delta_{p2} - \delta_{p1})^2 + (\delta_{h2} - \delta_{h1})^2}$$

When the R_{HSP} value between the solvent and the nonsolvent is calculated, a low value means

that the affinity between the two solvents is high, which can be expected to exhibit a fast solvent-nonsolvent exchange rate during the demixing process. Using this relationship, the membranes with various porous structures could be fabricated by changing the solvent and nonsolvent for one polymer.

Another main factor in determining the demixing process is the hydrophilicity or hydrophobicity of polymer. As above mentioned, the two demixing processes depend on the precipitation rate of the polymer.[19] In other words, the modification of the polymer can change the phase inversion behavior in a fixed solvent-nonsolvent system. In general, higher polymer concentration, the lower affinity between the solvent and nonsolvent, higher viscosity of the polymer solution will lead to slow solvent–nonsolvent exchange.

The NIPS methods are more complicated than the other phase inversion methods because there are too many parameters. In addition, the asymmetric porous structure containing finger-like macrovoids normally exhibits too low mechanical property to be utilized as a separator membrane practically. It is noteworthy, however, that the utility of the NIPS method increases due to its low processing temperatures and simple operation.

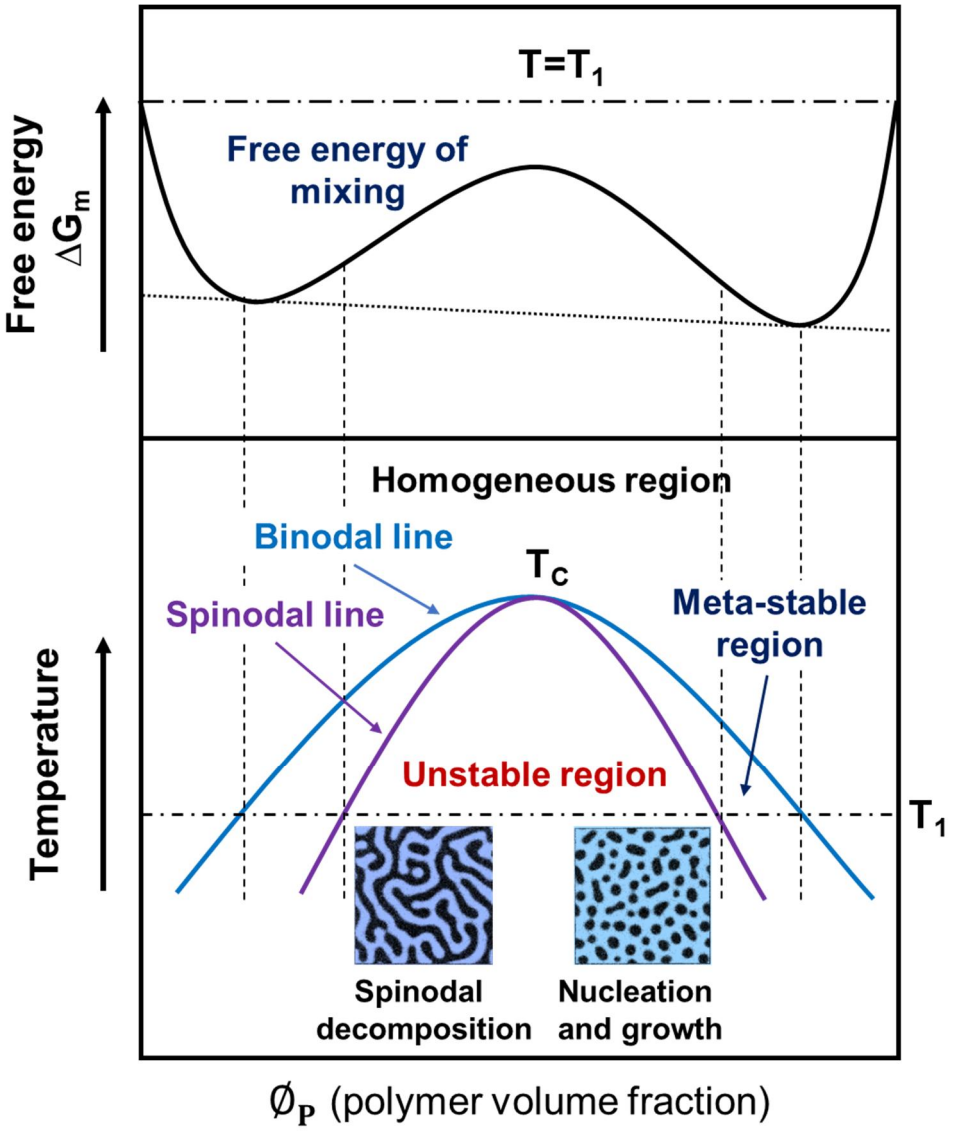

Figure 1-2. The schematic illustration of a phase diagram.

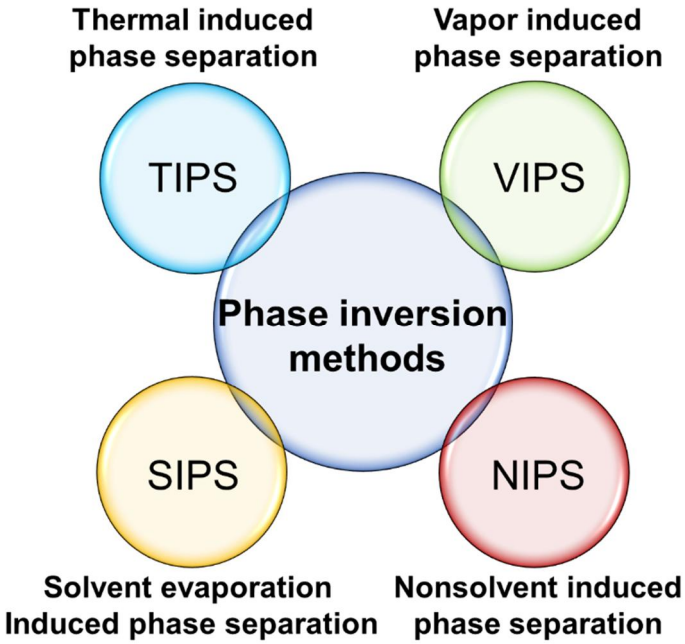

Figure 1-3. Various phase inversion methods as different physical ways of changing the thermodynamic states of the solution.

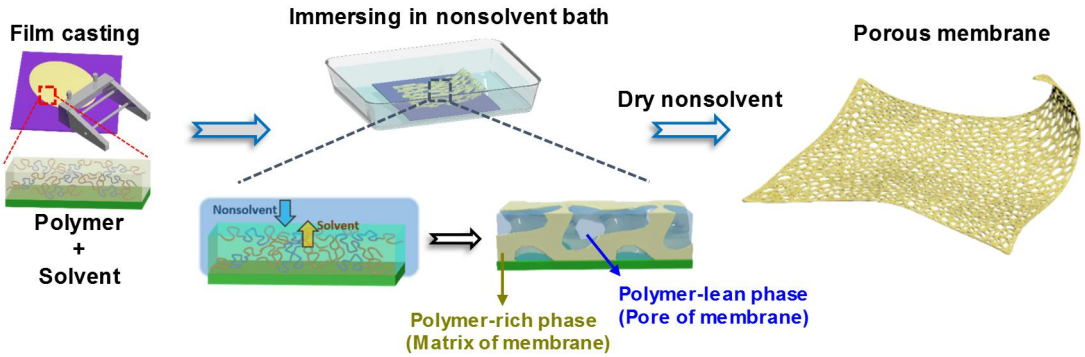

Figure 1-4. The typical fabrication process of porous membrane via NIPS method.

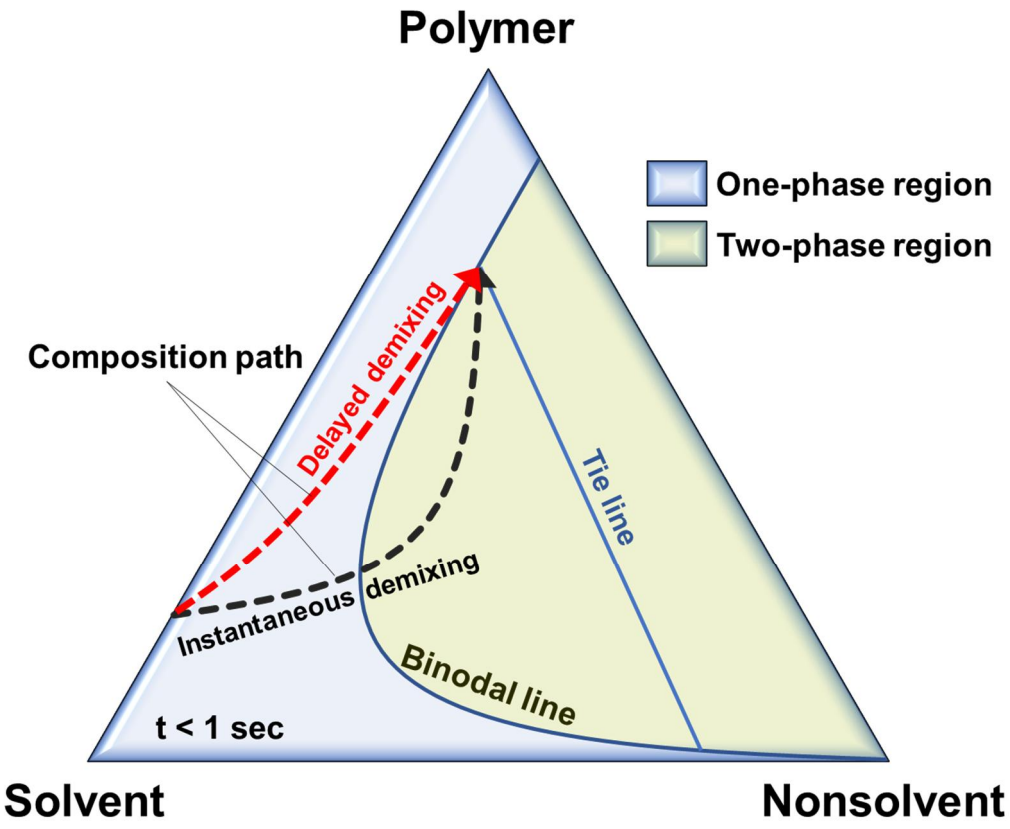

Figure 1-5. Ternary phase diagram of the NIPS method.

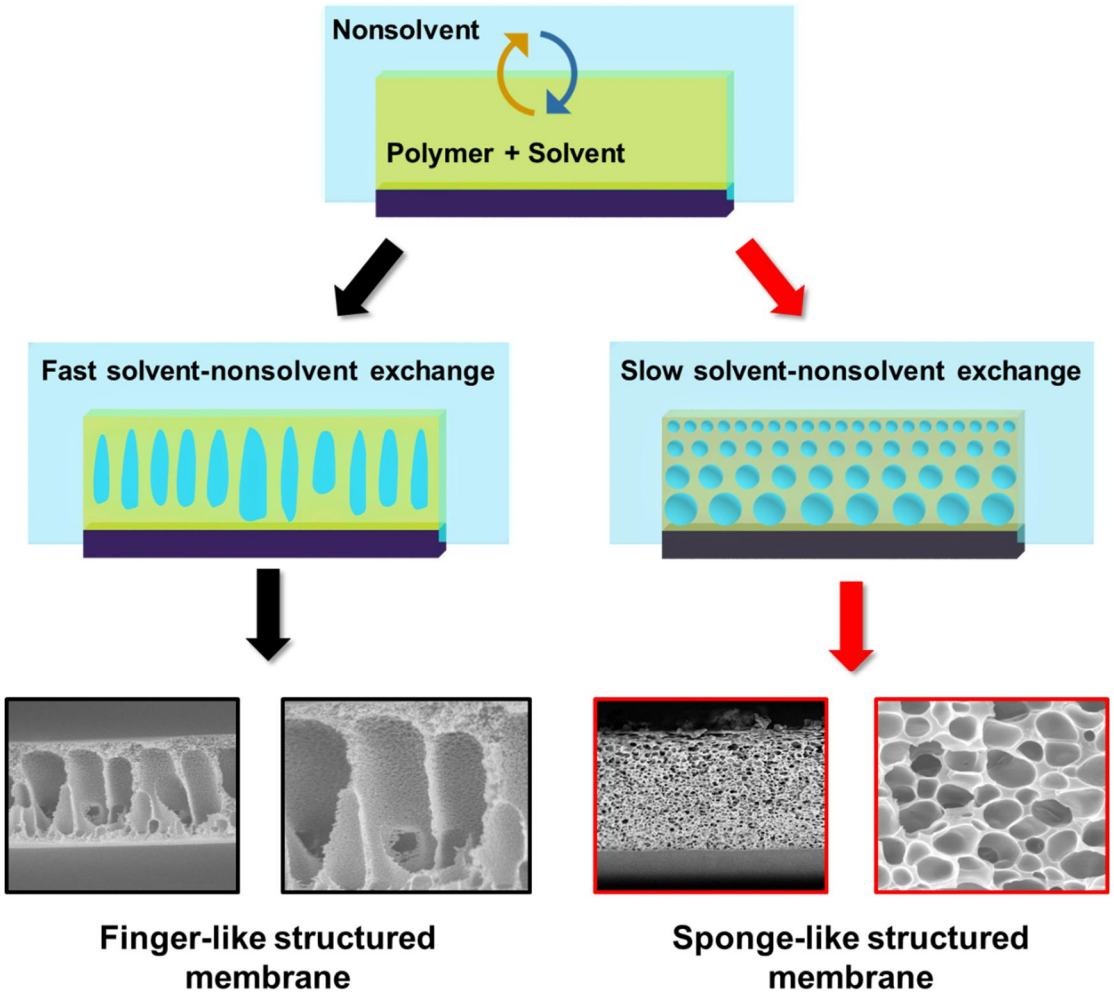

Figure 1-6. Two type of membrane morphologies caused by different solvent-nonsolvent exchange rate.

Solvents	Hansen parameters ($MPa^{1/2}$)			
	δ_d	δ_p	δ_h	δ_t
Aromatic hydrocarbons				
Benzene	18.4	0.0	2.0	18.6
Ethyl benzene	17.8	0.6	1.4	17.8
Toluene	18.0	1.4	2.0	18.2
Naphthalene	19.2	2.0	5.9	20.3
o-Xylene	17.8	1.0	3.1	18.0
Styrene	18.6	1.0	4.1	19.0
Alkanes				
n-Butane	14.1	0.0	0.0	14.1
n-pentane	14.5	0.0	0.0	14.5
n-Hexane	14.9	0.0	0.0	14.9
n-Octane	15.5	0.0	0.0	15.5
Cyclohexane	16.8	0.0	0.2	16.8
Ethers				
Tetrahydrofuran	16.8	5.7	8.0	19.4
1,4 Dioxane	19.0	1.8	7.4	20.5
Diethyl ether	14.5	2.9	5.1	15.8
Ketones				
Acetone	15.5	10.4	7.0	20.0
Methyl ethyl ketone	16.0	9.0	5.1	19.0
Cyclohexanone	17.8	6.3	5.1	19.6
Esters				
Ethylene carbonate	19.4	21.7	5.1	29.6
Methyl acetate	15.5	7.2	7.6	18.7
Ethyl acetate	15.8	5.3	7.2	18.1
Diethyl carbonate	16.6	3.1	6.1	17.9
methanol	15.1	12.3	22.3	29.6
Alcohols				
methanol	15.1	12.3	22.3	29.6
ethanol	15.8	8.8	19.4	26.4
1-propanol	16	6.8	17.4	24.5
2-propanol	15.8	6.1	16.4	23.5
1-butanol	16	5.7	15.8	23.1
2-butanol	15.8	5.7	14.5	22.2
Isobutanol	15.1	5.7	16.0	22.7
Cyclohexanol	17.4	4.1	13.5	22.4
Halo hydrocarbon				
Chloroform	17.8	3.1	5.7	19.0
Chlorobenzene	19.0	4.3	2.0	19.6
Water	15.6	16	42.3	47.8

Table 1. Hansen solubility parameters of several common solvents

1.3 Multifunctional separator membranes via phase inversion

When the NIPS is used, an asymmetrical porous morphology with a different pore size at the top and bottom are often developed. In practical battery applications, the asymmetrical structure often deteriorates the battery performance due to uneven ionic flow and different electrolyte absorption property.[27] Furthermore, the solvent-nonsolvent demixing normally develops finger-like pore (macro-voids) with low mechanical properties. Moreover, the optimization of fabrication conditions for developing a uniform porous structure is difficult because numerous factors affect the final membrane morphologies.[11] Despite these drawbacks, numerous researches have been conducted to fabricate the porous membrane via NIPS and used it as a separator membrane for energy storage devices due to its low cost, easy process, and the ability to utilize various polymers.[11,15,28-31]

In general, the conventional separator for the LIBs has mainly used polyolefin-based microporous membranes, which show several drawbacks such as poor thermal stability, low wettability, and poor electrolyte retention properties.[9] In order to overcome these problems, a variety of polymers such as polyacrylonitrile (PAN),[32-34] poly(vinylidene fluoride) (PVDF),[35-38] poly(methyl methacrylate) (PMMA),[39,40] poly(vinylidene fluoride-co-hexafluoropropylene) (PVDF-co-HFP),[41-43] polyimide (PI),[44] poly(phenylene oxide) (PPO),[45] poly(vinyl alcohol) (PVA)[46-48] have been used for preparing microporous membrane via phase inversion method.

The PAN membrane has been utilized as separators for LIBs due to its high thermal stability, good processability, excellent electrochemical stability, desirable structure for high electrolyte uptake, and good compatibility with electrodes. The PAN membranes can decrease the dendrite formation during the charge-discharge cycles of LIBs. Furthermore, The PAN also aids Li-ion transport owing to the interaction between the C≡N groups of PAN and Li-ion.[49,50] As a result, the PAN membranes exhibit good electrochemical stability and high ionic conductivity in LIBs. However, when the PAN membrane is immersed in the organic electrolyte for a long time, it loses its porous structure and turns into gel because the electrolyte absorbed in PAN, which reduces ionic conductivity.

The PVDF membrane is electrochemically and physiochemically stable in LIBs. The PVDF membranes have good wettability toward liquid electrolyte solution and strong mechanical properties. Magistris et al. fabricated the microporous PVDF membrane via NIPS process, which has sponge-like and finger-like pores.[37] They found that the LIBs with PVDF separator membrane shows high ionic conductivity due to high affinity between PVDF and electrolyte.

However, when the PVDF separator was used, LiF could be generated due to the interaction between the fluorine atoms in PVDF and lithium ions.[51]

The PMMA membrane is also fabricated for separators owing to its high affinity to the electrolyte. The PMMA membrane exhibits good electrochemical and thermal stabilities, high ionic conductivity and good adhesion to the electrodes owing to the formation of gel phases with liquid electrolyte. However, the PMMA exhibits low mechanical strength due to its amorphous nature.[52] The high crystallinity of the separator membrane is one of the main causes of the high internal resistance of LIBs. The separator with high crystalline region normally exhibits low discharge capacity and a poor rate capability because the crystalline region of the separator delays the migration of Li ions. In order to enhance the ionic conductivity and reduce the crystallinity, copolymers have been utilized for microporous separators such as PVDF-co-HFP membrane.

The PVDF-co-HFP is a promising material for the separator of LIBs because it shows good electrochemical stability, high affinity to the liquid electrolyte, and excellent adhesion with the electrodes. The crystalline PVDF region acts as mechanical support for the separator while the amorphous HFP region helps to take a large amount of liquid electrolyte. PVDF-co-HFP also has electron-withdrawing fluorine atoms in the polymer backbone and a high dielectric constant. These features are advantageous for dissociating lithium salt into Li-ions. Shi et al. fabricated the highly porous PVDF-co-HFP membranes by using the NIPS method and investigated the electrochemical properties of the membrane.[42] The manufacturing condition such as polymer solvent determined the porous structure, including pore size and porosity.

Along with monolayered membranes using the above-mentioned polymers, various studies have been carried out to apply the phase separation on the surface of conventional polyolefin-based separator membranes,[53] or to manufacture various composite membranes by phase separation with ceramic materials.[45,54,55] In most cases, they have proposed a separator with enhanced ionic conductivity and fast rate capability by modifying the hydrophobic property of the conventional separator membrane and by improving the wettability to the electrolyte. It is also reported that polymers, which cannot shrink easily at high temperatures, can protect the short circuit problem.

Although polymers can be modified to various functional groups, the most reported membranes have been prepared by polymer itself via NIPS. It is expected to play various beneficial roles in the operation of LIB cells by using a polymer with a various functional group. Therefore, it is necessary to develop a functional membrane that can solve the problems which devastating the battery performances and meet various requirements of conventional LIBs by combining various functional polymer materials and NIPS method together.

1.4 Reference

[1] J. M. Tarascon, M. Armand, *Nature* **2001**, *414*, 359.

[2] J. B. Goodenough, Y. Kim, *Chem. Mater.* **2010**, *22*, 587.

[3] D. Bruce, K. Haresh, T. Jean-Marie, *Science.* **2011**, *334*, 928.

[4] V. Etacheri, R. Marom, R. Elazari, G. Salitra, D. Aurbach, *Energy Environ. Sci.* **2011**, *4*, 3243.

[5] J. B. Goodenough, K. S. Park, *J. Am. Chem. Soc.* **2013**, *135*, 1167.

[6] C. Liu, F. Li, M. Lai-Peng, H. M. Cheng, *Adv. Mater.* **2010**, *22*, 28.

[7] B. Scrosati, J. Hassoun, Y. K. Sun, *Energy Environ. Sci.* **2011**, *4*, 3287.

[8] P. Arora, Z. Zhang, *Chem. Rev.* **2004**, *104*, 4419.

[9] H. Lee, M. Yanilmaz, O. Toprakci, K. Fu, X. Zhang, *Energy Environ. Sci.* **2014**, *7*, 3857.

[10] H. Strathmann, K. Kock, *Desalination.* **1977**, *21*, 241.

[11] G. R. Guillen, Y. Pan, M. Li, E. M. V. Hoek, *Ind. Eng. Chem. Res.* **2011**, *50*, 3798.

[12] S. Loeb, G. S.; Sourirajan, *Adv. Chem. Ser.* **1968**, *38*, 117.

[13] A. F. Ismail, L. P. Yean, *J. Appl. Polym. Sci.* **2003**, *88*, 442.

[14] I. M. A. ElSherbiny, A. S. G. Khalil, M. Ulbricht, *Adv. Mater. Interfaces.* **2019**, *6*, 1.

[15] S. Yoo, J.-H. Kim, M. Shin, H. Park, J.-H. Kim, S.-Y. Lee, S. Park, *Sci. Adv.* **2015**, *1*, e1500101.

[16] Y. Xia, J. Li, H. Wang, Z. Ye, X. Zhou, H. Huang, Y. Gan, C. Liang, J. Zhang, W. Zhang, *J. Solid State Electrochem.* **2019**, *23*, 519.

[17] H. Zhang, C. E. Lin, M. Y. Zhou, A. E. John, B. K. Zhu, *Electrochim. Acta* **2016**, *187*, 125.

[18] D. Li, H. Zhang, X. Li, *J. Memb. Sci.* **2018**, *565*, 42.

[19] J. Mulder, *Basic Principles of Membrane Technology*, Kluwer Academic, London, 2012.

[20] J. G. Wijmans, J. Kant, M. H. V Mulder, C. A. Smolders, *Polymer.* **1985**, *26*, 1539.

[21] S. S. Zhang, *J. Power Sources* **2007**, *164*, 351.

[22] W. Lu, Z. Yuan, Y. Zhao, H. Zhang, H. Zhang, X. Li, *Chem. Soc. Rev.* **2017**, *46*, 2199.

[23] P. J. Flory, *Principles of polymer chemistry*, Cornell Univ. Press, New York, 1953.

[24] C. M. Hansen, *An Introduction. In Hansen Solubility Parameters - A User's Handbook*, CRC Press BocaRaton, FL, 2000.

[25] R. F. Blanks, J. M. Prausnitz, *Ind. Eng. Chem. Fundam.* **1964**, *3*, 1.

[26] Hansen, C. M. Skaarup, K, *J. PaintTechnol*. **1967**, *39*, 511

[27] M. F. Lagadec, R. Zahn, V. Wood, *Nat. Energy.* **2019**, *4*, 16.

[28] W. Wei, H. Zhang, X. Li, H. Zhang, Y. Li, I. Vankelecom, *Phys. Chem. Chem. Phys.* **2013**, *15*, 1766.

[29] Y. Li, X. Li, J. Cao, W. Xu, H. Zhang, *Chem. Commun.* **2014**, *50*, 4596.

[30] J. Dong, Y. Zhang, J. Wang, Z. Yang, Y. Sun, D. Zeng, Z. Liu, H. Cheng, *J. Memb. Sci.* **2018**, *568*, 22.

[31] J. Il Kim, K. Y. Chung, J. H. Park, *J. Memb. Sci.* **2018**, *566*, 122.

[32] H.-S. Min, J.-M. Ko, D.-W. Kim, *J. Power Sources.* **2003**, *119–121*, 469.

[33] F. Groce, F. Gerace, G. Dautzemberg, S. Passerini, G. B. Appetecchi, B. Scrosati, *Electrochim. Acta.* **1994**, *39*, 2187.

[34] G. B. Appetecchi, F. Croce, B. Scrosati, *J. Power Sources.* **1997**, *66*, 77.

[35] F. Boudin, X. Andrieu, C. Jehoulet, I. I. Olsen, *J. Power Sources.* **1999**, *81–82*, 804.

[36] J. Saunier, F. Alloin, J. Y. Sanchez, G. Caillon, *J. Power Sources.* **2003**, *119–121*, 454.

[37] A. Magistris, P. Mustarelli, F. Parazzoli, E. Quartarone, P. Piaggio, A. Bottino, *J. Power Sources.* **2001**, *97–98*, 657.

[38] G. L. Ji, B. K. Zhu, Z. Y. Cui, C. F. Zhang, Y. Y. Xu, *Polymer.* **2007**, *48*, 6415.

[39] O. Bohnke, G. Frand, M. Rezrazi, C. Rousselot, C. Truche, *Solid State Ionics.* **1993**, *66*, 97.

[40] G. B. Appetecchi, F. Croce, B. Scrosati, *Electrochim. Acta.* **1995**, *40*, 991.

[41] A. Magistris, E. Quartarone, P. Mustarelli, Y. Saito, H. Kataoka, *Solid State Ionics.* **2002**, *152–153*, 347.

[42] Q. Shi, M. Yu, X. Zhou, Y. Yan, C. Wan, *J. Power Sources.* **2002**, *103*, 286.

[43] S. S. Zhang, K. Xu, D. L. Foster, M. H. Ervin, T. R. Jow, *J. Power Sources.* **2004**, *125*, 114.

[44] J. Tan, L. Kong, Z. Qiu, Y. Yan, *J. Solid State Electrochem.* **2018**, *22*, 3363.

[45] Y. Lv, B. Gu, *J. Mater. Sci. Mater. Electron.* **2017**, *28*, 6512.

[46] C. He, J. Liu, J. Li, F. Zhu, H. Zhao, *J. Memb. Sci.* **2018**, *560*, 30.

[47] W. Xiao, L. Zhao, Y. Gong, J. Liu, C. Yan, *J. Memb. Sci.* **2015**, *487*, 221.

[48] W. Xiao, K. Zhang, J. Liu, C. Yan, *J. Mater. Sci. Mater. Electron.* **2017**, *28*, 17516.

[49] K. M. Abraham, *J. Electrochem. Soc.* **2006**, *137*, 1657.

[50] Rokeya Huq, Rene Koksbang, P. E. Tonder and Gregory C. Farrington, Electrochim. Acta. **1992**, 37, 9, 1681

[51] A. Du Pasquier, *J. Electrochem. Soc.* **1998**, *145*, 472.

[52] A. Manuel Stephan, K. S. Nahm, *Polymer.* **2006**, *47*, 5952.

[53] Y. Li, H. Pu, *J. Power Sources.* **2018**, *384*, 408.

[54] J. Cui, J. Liu, C. He, J. Li, X. Wu, *J. Memb. Sci.* **2017**, *541*, 661.

[55] C. M. Costa, M. Kundu, V. F. Cardoso, A. V. Machado, M. M. Silva, S. Lanceros-Méndez, *J. Memb. Sci.* **2018**, *564*, 842.

Chapter . Highly Stretchable Separator Membrane for Deformable Energy Storage Devices

2.1 Introduction

There has been growing interest in stretchable electronic devices owing to their potential applications in wearable electronics, implantable medical devices, and electronic skins.[1-3] To fulfill the demand for reliable stretchable electronic devices, a key challenge is the development in shape of deformable energy storage devices for supplying power to them.[4] Up to date, several studies have successfully achieved the deformable power sources such as stretchable lithium-ion batteries (LIBs), stretchable supercapacitors, and stretchable silver-zinc batteries.[5-8] Most of them mainly focused on the development of deformable current collectors (e.g., embedding conductive materials in soft substrates or elastic substrates)[9,10] or structural layouts (e.g., helically coiled spring design, serpentine interconnected configuration, and origami structure).[11-13]

In comparison, a stretchable separator membrane for deformable energy storage devices attracts little attention. The separator membrane is basically used to prevent physical and electrical contact between electrodes while offering an ion conduction channel.[14] Various types of stretchable batteries are being developed, and thus the stretchable properties of the separator membrane are also required. Generally, because ionic gel-polymer electrolytes (GPEs) are easily controllable and sufficiently deformable, they have been employed as the separator membrane in deformable energy storage devices.[13,15,16] Although ion-conducting GPEs can be used as both electrolyte and separator, they have intrinsically lower ionic conductivity than liquid electrolytes[17] and poor mechanical properties which are likely to cause an internal short problem due to the contact of both electrodes under physical deformation.[18,19] In order to fabricate a reliable stretchable energy storage device without these limitations, the presence of a physical separation barrier having an ion-conducting channel and stretchability is essential. Recently, Liu et al. reported a stretchable separator membrane for wavy structured stretchable LIBs using electrospinning techniques.[20] Li et al. also used electrospinning process to fabricate a stretchable polyurethane separator for stretchable supercapacitor.[21] However, electrospinning has critical drawbacks such as the use of complex equipment, slow production rate, and possible toxicity of chemical residues in electrospun fibers. Moreover, it has the limitation for large-scale production for industry level due to its high cost.[22,23] Given these limitations, it is still necessary to develop

and improve the fabrication methodologies for stretchable separator membranes. Although various attempts have been made in the membrane component to achieve the complete stretchability of the battery, the development of the standardized separator membrane that can be applied to various types of stretchable battery has not yet been reported. Therefore, the development of stretchable separator membranes with high processibility and wide versatility is essential for the realization of a fully stretchable battery.

Nonsolvent induced phase separation (NIPS) represents one of the most promising fabrication methods for various porous membranes such as energy-storage devices (specially LIBs[24-26]), redox flow batteries,[27] reverse osmosis membrane,[28] and gas separations[29] owing to the scalable fabrication, morphology control for various requirements, and a wide selection of materials.[30] In NIPS, the porous membrane structure can be developed by controlling the phase separation between polymer and solvent in thermodynamic and kinetic aspects.[31] Usually, a co-diffusion of solvent and nonsolvent during phase inversion induces fingerlike voids in the membrane, which is inappropriate to use for deformable energy devices due to low mechanical properties of the as-made separator under physical deformation.[32] Moreover, the optimization of conditions to develop uniformly porous structure is difficult because various factors affect the final membrane structure. For these reasons, despite the advantageous characteristics mentioned above, the fabrication of a reliable stretchable separator membrane via the NIPS method has not yet been reported.

Here, based on poly(styrene-*b*-butadiene-*b*-styrene) (SBS) block copolymer that is thermoplastic elastomer (TPE) having high stretchability and recyclability, we report a stretchable separator membrane for deformable energy storage devices *via* a facile and scalable NIPS (referred to as SBN separator membrane; stretchable block copolymer based membrane by using NIPS). We precisely controlled several key parameters of NIPS for tailoring porosity and mechanical properties of the SBN separator membrane, resulting in high stretchability (270% to the uniaxial direction, 60% to the biaxial direction) and a high porosity of 60%. To the best of our knowledge, it is the first report on the fabrication of the stretchable separator membrane using NIPS process. As a demonstration, we investigated their electrochemical performances as a stretchable separator membrane both in deformable LIB systems based on an organic electrolyte and an aqueous electrolyte (as referred to in the following as LIBs and aqueous rechargeable lithium-ion batteries (ARLBs), respectively).

When it was evaluated as a separator membrane for LIBs, the SBN membrane displayed stable cycle retention (87% after 100 cycles at a rate of 1 C) under 100% strain. Furthermore, when it was used for stretchable ARLBs, the stretchable batteries showed stable cycle retention (80% after 200 cycles at a rate of 10 C), and provide a sufficient power to light up a light-emitting

diode (LED), even under a repeated strain and released state of 100%. The SBN separator membrane could open up new possibilities as a widely applicable stretchable porous separator membrane for a stretchable power source.

2.2 Experimental

Fabrication of stretchable separator membrane

SBS solution dissolved in THF was cast on a flat silicon substrate using a doctor blade with a gap of 300 μm ± 10 μm and then immediately immersed in the nonsolvent coagulation bath for 6 h at room temperature. During the phase separation process, transparent cast film turned to be opaque. After sufficient solvent-nonsolvent exchange, the film was dried in a vacuum oven at 70 °C for 20 min to remove the solvent. Finally, oxygen plasma treatment (Femto plasma cleaner, 100W) was carried out for removing the dense skin layer on both top and bottom surfaces of the films.

Deformable organic electrolyte-based LIB test

The electrolyte was 1 M $LiPF_6$ with ethylene carbonate/polycarbonate (EC/PC, 50/50 vol.%, Panax Etec). The aluminum laminated film was used as the packaging material (WBCS 3000 battery system, Wonatech). The anode, cathode, and stretchable separator membrane were assembled into a pouch-type full cell in the Ar-filled glove box. The full batteries were tested at a rate of 0.2-3 C between a cutoff range of 1 and 2.6 V. The mass ratio of cathode and anode materials was designed as 1:1.2. The loading density of full batteries was 1.5 mg cm^{-2}. The flexible cathode and anode were prepared by a previous method.[46] During the electrochemical measurements, the flexible full cell was folded at the desired angle using a bending machine. In order to demonstrate the performance of the SBN separator membrane in the stretched state, we assembled the pouch-type full batteries. Firstly, an anode (using LTO as active material) with nickel tap was attached to the packaging material. And then, one of the SBN separator membranes was fixed by the PI tape on the pre-fixed electrode and the other side was artificially stretched and fixed with PI tape. And cathode (using LFP as active material) was fixed on the 100% prestrained SBN separator membrane. Lastly, vacuum packaging of the pouch-type full cell was conducted after the EC/PE electrolyte injection.

Stretchable aqueous LIB test

The stretchable electrode was fabricated by a previous method.[44] The active materials (LMO@CNT and PI@AC) were coated by spray coating method on a hot plate. The stretchable cathode and anode were assembled with a stretchable separator membrane. The Ecoflex 0030 was used as the packaging material and a spacer. The electrochemical performance of the stretchable ARLBs was measured using an electrochemical analyzer (VSP, Biologic science instruments)

with a 1 M Li_2SO_4 aqueous electrolyte. The full cell was conducted between cut off voltage of 0 and 2 V. The two stretchable ARLBs were connected in series and tested between cut-off voltage of 0 and 4 V. The mass ratio of cathode and anode materials was designed as 1:1.3. During the electrochemical measurements, the stretchable full batteries were stretched using the tensile strength machine.

Characterization

The tensile strength was conducted by a tensile strength machine (Petrol LAB DA-01). The morphology of the stretchable separator membrane was investigated by a scanning electron microscope (SEM, FEI Verios 460). For the wettability measurements to the liquid electrolyte, oxygen plasma was carried out using the Femto plasma cleaner and contact angle was measured using a drop shape analyzer (DSA-100, KRÜSS GmbH). After the oxygen plasma treatment, the surface hydroxyl group and carbonyl group were examined using a FTIR spectrometer (670-IR, Agilent). The air permeability of the stretchable separator membrane was measured using a Gurley densometer (4110N, Gurley). The porosity measurement of the SBN separator membrane was conducted by weighing the SBN separator membrane for several times before and after immersing the n-butanol for 30 min. Before putting the SBN separator membrane into n-butanol, volume and weight were measured, and then it was soaked for 30 min. After that, the SBN separator membrane was taken out and weighed, and this process was repeated several times to calculate porosity.

2.3 Results and discussion

The overall fabrication processes for the SBN separator membrane are schematically illustrated in **Figure 2-1a**. First, SBS block copolymer dissolved in a solvent was casted into a film by a doctor blade onto a flat silicon substrate. Subsequently, when the film was immediately immersed in a nonsolvent that is miscible with the solvent for the NIPS process, a demixing (liquid-liquid separation) occurred in the coagulation bath. The thermodynamic equilibrium of polymer film began to be disturbed and transformed single phase into two phases consisting of polymer-rich and polymer-poor phases, eventually forming the membrane matrix and pores.[33] After the phase inversion was completed, it was dried at 70 ºC for 20 min in a vacuum chamber, resulting in the formation of a three-dimensional (3D) porous structured membrane. Next, oxygen plasma treatment was used to remove the dense layer on both top and bottom surfaces of the membrane. Finally, a self-standing SBN separator membrane was obtained. To demonstrate the deformability of the as-fabricated SBN separator membrane, we conducted the uniaxial **(Figure 2-1b)** and biaxial stretching tests (**Figure 2-1c)**. It indicated that the SBN separator membrane was successfully achieved up to 200% uniaxial stretching as well as 60% biaxial stretching without mechanical damage.

Porous structures of membranes prepared by the NIPS method are mainly determined by the thermodynamic and kinetic aspects of the polymer chains in nonsolvent. Although there are many factors that affect the final membrane structures, it can be controlled by adjusting the main components (e.g, polymer, solvent, and nonsolvent). In a previous study, Strathmann et al. elucidated a thermodynamic behavior of demixing through a ternary phase diagram.[34] In the ternary phase diagram (**Figure 2-2a**), there are three components (polymer, solvent, and nonsolvent) at the corners of the triangle and two regions including a one-phase region and two-phase region divided by the binodal line, which is calculated based on the Flory-Huggins thermodynamics.[35] The position of phase boundary is determined by the interactions among the three components. Inside the binodal line, two phases (including polymer-rich and polymer-lean phase) have thermodynamic equilibrium to each other and exist as different compositions. When the as-cast polymer thin film is immersed into the nonsolvent, the chemical potential gradient of polymer film induces a solvent exchange between solvent and nonsolvent in the coagulation bath. The exchange rate of solvent and nonsolvent is an important factor to determine the two demixing behaviors, which can be expressed by different composition paths after immersion in a nonsolvent bath as schematically illustrated in **Figure 2-2a**. A fast solvent-nonsolvent exchange causes the transition from homogeneous one-phase region to two-phase one immediately after immersion

(**Figure 2-2a**, red line), which is called instantaneous demixing, leading to the large fingerlike structure membrane. The fingerlike pores make membrane brittle and asymmetric structure due to their nonuniform shapes. Meanwhile, a slow solvent exchange does not demix immediately upon immersing in the coagulation bath (**Figure 2-2a**, purple line), resulting in the formation of spongelike morphology with small pores, which is called a delayed demixing.[31] In terms of a stretchable separator membrane, although large macro voids accelerate a fast ion transfer, they easily cause a low mechanical strength and a self-discharging problem due to an electrical leakage through the macro voids and an internal short-circuit problem under mechanical deformation.[14,36,37] For these reasons, the spongelike structure membranes are particularly suitable for deformable energy storage devices.

The interaction between solvent and nonsolvent mainly affects the demixing rate, suggesting that the choice of suitable solvent and nonsolvent is important to fabricate the desired porous structure. To find the adequate solvent-nonsolvent pair which can develop spongelike pore morphology for the deformable separator, firstly, we controlled various nonsolvents having different solubility parameters. In the ternary system, the thermodynamic interactions are directly affected by the solubility parameter difference between the components. The Hansen solubility parameter (HSP) is mainly used to calculate the affinity between two different materials. The HSP can be divided into three parts, including a dispersion force component (δ_d), a polar component (δ_p), and a hydrogen bonding component (δ_h).[38] The relative miscibility between the solvent and nonsolvent can be easily predicted by calculating the HSP distance, R_{HSP}, using the following equation (1):[39]

$$R_{HSP} = \sqrt{4(\delta_{dS} - \delta_{dNS})^2 + (\delta_{pS} - \delta_{pNS})^2 + (\delta_{hS} - \delta_{hNS})^2} \quad (1)$$

where the subscripts "S" and "NS" stand for solvent and nonsolvent, respectively. The HSP of solvent and nonsolvents are summarized in **Table S2-1**. The R_{HSP} value of tetrahydrofuran (THF)–n-butanol pair (31.7 $MPa^{1/2}$) is the smallest, which indicates that THF is more miscible with n-butanol than other nonsolvents. The high miscibility between solvent and nonsolvent implies that faster solvent-nonsolvent exchange occurs in the coagulation bath than other pairs. The R_{HSP} values of THF with n-propanol, ethanol, methanol, and water pairs are 46.1, 71.8, 129.8, and 644.2 $MPa^{1/2}$, respectively (**Figure 2-2b**). The high R_{HSP} value of solvent-nonsolvent pair indicates a low miscibility between them, resulting in a slow solvent-nonsolvent exchange rate.

To investigate the top layer and cross-sectional morphologies of the as-made SBN separator membrane fabricated by different nonsolvents at the same SBS polymer concentration (6 wt%) and O_2 plasma time (35 min), scanning electron microscopy (SEM) analysis was carried out. As expected from the R_{HSP} values, the low miscibility between solvent and nonsolvent developed the dense membrane having very small pores (under 500 nm), especially ethanol (**Figure 2-2c, d)**.

And SEM images of the SBN separator membrane made by n-propanol are shown in **Figure 2-2e** and **f**. Top and bottom surfaces had larger pores than those of ethanol nonsolvent. The cross-sectional view showed micron-size pores (about 1~2 μm) in the resulting membrane affected by the high miscibility between solvent and nonsolvent. Lastly, **Figure 2-2g** and **h** shows the top view and cross-sectional SEM images of the SBN separator membrane developed by n-butanol nonsolvent. As shown in the value of R_{HSP} **(Figure 2-2b)**, n-butanol has higher miscibility with THF compared with other nonsolvents, resulting in the formation of large pores. Interestingly, the above alcohol-based nonsolvents did not provide instantaneous demixing with THF, which induced the fingerlike pores in the membrane.

In order to determine the tortuosity of pores, we conducted Gurley analysis to estimate the time required for a certain amount of air passing through a defined area of the membrane under a specified pressure. Although many pores existed in the membrane, the interconnection of pores was important for the good pathway of ions. The Gurley values of the SBN separator membrane fabricated by n-propanol and n-butanol were 1200 and 210 s/100 cc air, respectively (**Figure S2-1**). Considering that polyolefin separators (e.g., polyethylene, polypropylene) for commercial energy storage devices have the Gurley value of about 200~300 s/100 cc air, the SBN separator membrane formed by n-butanol nonsolvent showed a proper permeability, which can be applicable to the commercial energy-storage system. Although the separators having a high Gurley value provide effective internal short-circuit protection, alleviation of liquid electrolyte leakage, and a self-discharge problem, they can result in the low ion transport and internal resistance in energy storage device.[14] Hence, it is important to have an appropriate Gurley value required for various energy storage devices. The experimental results clearly showed that the small R_{HSP} between the solvent and nonsolvent induced larger pore size which can offer high permeability. In other words, the control of solvent-nonsolvent pair greatly influences the pore size of the spongelike membrane ranging from 500 nm to 2 μm. In the manufacturing method of stretchable separator membrane using the NIPS, n-butanol is a viable candidate as the nonsolvent in the SBS block-copolymer/THF system.

A certain area of the film needs to be manufactured to serve as the separator membrane. The as-cast polymer film, however, cannot maintain its original shape during the phase inversion step in the ethanol and methanol coagulation bath. The miscibility between solvent and nonsolvent and the affinity between polymer and nonsolvent are important in the membrane formation.[31] As nonsolvent power increased to the polymer (an increase of the solubility parameter difference between polymer and nonsolvent), precipitation and aggregation of polymer might be the dominant factor in forming the membrane. Once the SBS film was immersed in ethanol and methanol coagulation bath, the SBS block copolymer was quickly aggregated into a film that was

divided into pieces. Furthermore, the immersed film was immediately precipitated in the water coagulation bath due to the lowest affinity between water and SBS copolymer. Thus, the SBS film was firmly attached to the support after being immersed sufficiently in the nonsolvent bath.

The NIPS process normally develops dense layers on the top and bottom surface,[31] which disturbs the ionic transport between both electrodes. Oxygen plasma treatment on the polymer surface is a typical method to enhance the wettability against electrolyte by introducing hydrophilic functional groups. To understand the effect of O_2 plasma on polymer film surface, we used Fourier transform infrared spectroscopy (FTIR) for O_2 plasma treated and the untreated SBN separator membrane as shown in **Figure S2-2**. We clearly confirmed the formation of oxygenic functional groups (i.e., -OH and -COOH) on the surface of separator membrane.[40] These functional groups on the surface of the separator membrane greatly enhanced the ability of separator membrane uptaking polar electrolytes (**Figure S2-3)**.[41] Furthermore, it demonstrated that the dense layer on the top surface was physically etched by the oxygen plasma. SEM analysis was performed to observe surface morphologies of the SBN separator membrane (6 wt% polymer solution, referred to as SBN6) as a function of plasma treatment time ranging from 5 to 50 min (referred to as SBN605, SBN620, SBN635, and SBN650, respectively) as shown in **Figure S2-4**. However, excessive oxygen plasma treatment causes poor mechanical properties of the SBN separator membrane due to the removal of polymeric frame and scission of polymer chains.[41] Therefore, optimal plasma time is required, considering the mechanical properties of the SBN separator membrane. To characterize the mechanical properties of the SBN6 separator with different oxygen plasma time, tensile strength test was conducted. As a result, the stretchability of SBN6 separator was decreased by increasing plasma time **(Figure S2-5)**. We also measured the Gurley values of the oxygen plasma-treated SBN6 separator at different time periods to confirm the sufficient treatment time which can remove the surface dense layer. **Figure S2-6** clearly demonstrates that the SBN6 with less oxygen plasma treatment exhibited a high Gurley value, indicating that the surface dense layer still remained. From these results, the SBN635 separator with plasma treatment of 35 min was chosen as the optimal plasma time to ensure sufficient removal of the dense layer and a certain degree of stretchability.

The polymer concentration in the casting solution is another factor affecting membrane morphologies. Next, we controlled polymer concentration to adjust the porosity and mechanical properties of the SBN separator membrane that was made by THF and n-butanol pair with O_2 plasma treated for 35 min. When high polymer concentration was used, the final membrane structure showed a low porosity due to the high-volume fraction of the polymer.[32] Furthermore, it enabled to control the intrinsic rubbery properties of SBS copolymer for the stretchable separator membrane application. To investigate the influence on the surface morphology at

various SBS polymer concentrations, SEM analysis was conducted as shown in **Figure 2-3a-c**. The SBN thickness clearly increased as the polymer concentration changed from 6 to 10 wt% (referred to as SBN635, SBN835, and SBN1035, respectively).

To investigate the porosity changes of the SBN separator membrane having different polymer concentrations, the void volume of each sample was measured.[42] We calculated the porosity by weighing the SBN separator membrane before and after immersing in n-butanol, in which occupying volume is equal to the pore volume of the separator, as the following equation (2):[14]

$$\text{Porosity } (\%) = \left(\frac{W-W_0}{\rho_L V_0}\right) \times 100 \quad (2)$$

where W_0 and W represent the weight of the separator before and after the absorption of n-butanol, respectively, ρ_L is the density of n-butanol (0.81 g/cm^3), and V_0 is the geometric volume of the separator. As the SBS polymer concentration increased, the porosity of SBN decreased from 61% to 35%, resulting in the increase of Gurley value of SBN from 200 to 5000 s/100 cc as shown **Figure 2-3d**. The highlighted region shows a typical porosity in LIB separators ranging from 40% to 65% and the Gurley values ranging from 200 to 360 s/100 cc air, when commercial polyolefin separators were measured at the same Gurley equipment. The control of SBS concentration indicates a trade-off between the porosity and the Gurley values. From the porosity and Gurley of the SBN separator membrane, SBN635 exhibited a reasonable porosity and Gurley values compared with the others.

Next, to characterize the mechanical properties of separators having different SBS concentrations, we conducted the tensile strength test under the same conditions and compared with that of a commercial glass fiber (GF) separator in **Figure 2-3e**. The SBN separator membranes exhibited extremely high stretchability due to the inherent elastic property of TPE, contrary to the inorganic borosilicate based GF separator. Furthermore, the SBN635 separator membrane maintained the porous structure even uniaxial stretching up to 100% (**Figure S2-7**). By increasing SBS polymer concentration, the tensile strength and elongation at break of the SBN separator membrane simultaneously increased from 270% up to 470% owing to the low void volume ratio in the thick membrane. The stretchable separator membrane should be highly stretched and act as an ion conduction pathway. Thus, high stretchability of SBN was unsuitable for the separator membrane due to its high Gurley and low porosity, which typically hindered the ion conduction between an anode and a cathode. As an adequate SBS polymer concentration on the aspects of porosity, Gurley, and stretchability, the SBN635 separator membrane was selected as an available candidate for the stretchable separator membrane.

Mechanical durability of SBN separator membrane is also important for realizing the stretchable separator membrane. Thus, we measured the tensile strength of the SBN635 separator

membrane for 100 stretch/release cycles under a strain of 100% (**Figure 2-3f**). The maximum strain was applied at 100%, which is the same strain required at the joint of the human body.[43] During 100 cycles, the decrease of tensile strength was stabilized after 20 cycles. This demonstrates that the SBN635 separator membrane can function reliably as a separator even with multiple 100% strain cycles.

In our previous study, we fabricated stretchable ARLBs using conductive polymer composites as stretchable electrodes containing multidimensional conductive fillers.[44] This stretchable battery, where cathode and anode were coplanar electrode design without the separator, successfully supplied power even under 100% strain. However, this layout has a limitation in volumetric energy density (Wh/L_{device} with L_{device} = total volume) because the total battery volume of conventional configuration with the stacked electrode was smaller than that of the coplanar layout **(Figure S2-8)**. In this study, we introduced the optimized SBN separator membrane to the ARLBs for demonstrating the reliable stretchable energy storage device having high energy density. In addition, the fabricated SBN separator membrane was applied to the LIB system to confirm the applicability of various deformable energy storage devices based on organic and aqueous electrolytes.

At first, to investigate the electrochemical performance of the SBN635 separator membrane based on the organic electrolyte system, we fabricated the LIBs containing lithium titanate ($Li_4Ti_5O_{12}$ (LTO), as an anode) and lithium iron phosphate ($LiFePO_4$ (LFP), as a cathode) with 1 M $LiPF_6$ in EC/PC (v/v, 1/1) electrolytes. The cyclic voltammetry (CV) of SBN6 separator membrane with symmetric cell clearly demonstrated the electrochemical stability of the separator in the range of voltage window from 1 to 4 V at a scan rate of 2 mV s^{-1}. As shown in **Figure 2-4a**, the galvanotactic charge-discharge curves of full batteries with the SBN635 separator membrane were similar to that of a commercial GF separator. The voltage profiles, thus, showed the typical electrochemical feature of LTO//LFP full batteries. The overpotential of the full batteries with SBN6 separators membrane treated for different plasma time periods and the commercial GF separator was presented in **Figure S2-9**. As the plasma treatment time was increased from 10 to 35 min, the overpotential of charge-discharge was decreased from 330 to 102 mV, resulting in that the overpotential of the SBN635 separator membrane was similar as that of the commercial separator (~100 mV). From these results, the plasma treatment improved the ability to uptake electrolytes and increased the porosity of the separator, increasing Li-ion transport during charge and discharge. Furthermore, the separator did not change its morphology in organic electrolytes **(Figure S2-10)**. Thus, these results demonstrate that the SBN635 separator membrane was a suitable for LIB system based on organic electrolytes.

Figure 2-4b shows that the rate capability of the full cell with various SBN separator membranes was evaluated at various current densities of 0.2 C, 0.5 C, 1 C, and 3 C rate. When we applied a relatively high current of 3 C to the full cell, the specific capacity of SBN635 and GF separators exhibited the same features. However, the capacity of the SBN635 separator membrane was higher than that of SBN835, because the SBN635 separator membrane had a higher porosity than the SBN835 separator membrane (**see Figure 2-3e**). **Figure 2-4c** shows the cycling performance for the full batteries having both SBN635 and GF separators at a rate of 1C/1C (charge/discharge) for 300 cycles. The SBN635 separator membrane displayed a discharge capacity of above 110 mA h g^{-1}, which corresponded to an outstanding capacity retention of 87 % for 300 cycles. After the cycling test, we examined the mechanical stability of the SBN635 separator membrane that maintained its morphology without structural defects and disruption as shown in **Figure S2-11.** The GF separator, however, exhibited a gradual decay in the capacity of 92 mA h g^{-1} after 300 cycles due to side reactions with the hydrofluoric acid in $LiPF_6$ based electrolytes **(Figure S2-12)**.[45] Pouch-type foldable full batteries were fabricated to demonstrate the possibility of the SBN635 separator membrane for foldable LIBs (**Figure S2-13)**. Notably, the capacity of the foldable batteries retained well without losing their electrochemical performance.

In order to verify the applicability of the SBN separator membrane to stretchable LIBs based on organic electrolyte system, the full cell was fabricated using the 100% prestrained SBN635 separator membrane (**inset of Figure 2-4e and Figure S2-14**). More details about the fabrication procedures were summarized in the Experimental Section. Because the reliable model of the stretchable LIBs has not been yet developed, electrochemical tests were conducted using the prestrained SBN635 separator membrane in the typical pouch cell. **In Figure 2-4d**, the galvanostatic charge-discharge curves of full batteries composed of 100% prestrained SBN635 separator membrane indicated typical voltage profiles of LTO//LFP full batteries. However, overpotential plateaus of the pre-stretched SBN635 separator membrane were lower than that of the unstretched SBN separator membrane, because the thickness of the SBN separator membrane was decreased from 50 to 25 μm under 100 % strain (**inset of Figure 2-4d and Figure S2-7**). **Figure 2-4e** exhibits the excellent cycling performance of the full batteries equipped with the prestrained SBN separator membrane at a rate of 1 C for 100 cycles. Interestingly, these results demonstrate that SBN635 separator membrane successfully performed physical barrier to prevent the electrical contact between electrodes and ionic conducting channel even under 100% strain.[46]

To further demonstrate the possibility of the fabricated SBN635 separator membrane for stretchable energy devices, we constructed stretchable ARLBs consisting of a polyimide-coated

activated carbon (PI@AC) as an anode, SBN635 separator membrane, and $LiMnO_2$-coated carbon nanotube (LMO@CNT) as a cathode having 1 M Li_2SO_4 aqueous electrolyte. Furthermore, CV profiles SBN separator indicated no appreciable reactions in operating range of ARLBs**.** **Figure 2-5a** shows the charge-discharge profiles with the separator at 10 C under voltage window between 0 and 2 V. It showed that the capacity of the full ARLBs was 104 mA h g^{-1} with a coulombic efficiency of 93%. In **Figure 2-5b**, the cycling performance of full batteries was measured at a rate of 10 C. The ARLBs having the SBN635 separator membrane exhibited stable cycle retention of 80% after 200 cycles.

Figure 2-5c shows a practical application of the assembled stretchable ARLBs (PI@AC//SBN635//LMO@CNT) as a stretchable energy-storage device. Under a strain of 100%, the capacity retention of the stretchable ARLBs having the SBN635 separator membrane was 85% after 30 cycles. In **Figure 2-5d**, the optical images demonstrate that the as-assembled stretchable ARLBs connected in series can successfully power a red LED even under a strain of 100%, indicating the stretchability of the SBN635 separator membrane for practical use. These results clearly imply that our fabricated SBN635 separator membrane *via* NIPS method can be used for various deformable energy storage devices.

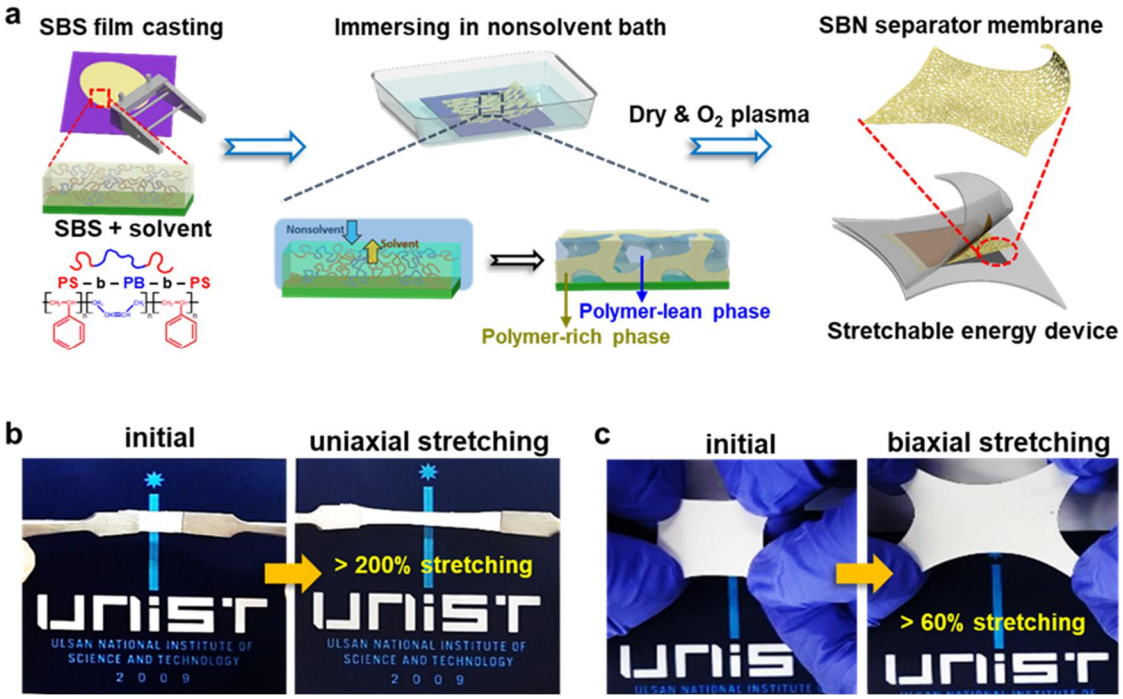

Figure 2-1. Fabrication process and digital photographs of the SBN separator membrane. a) Schematic illustration of an overall fabrication process based on NIPS method. Digital photographs of the SBN separator membrane under b) uniaxial stretching and c) biaxial stretching.

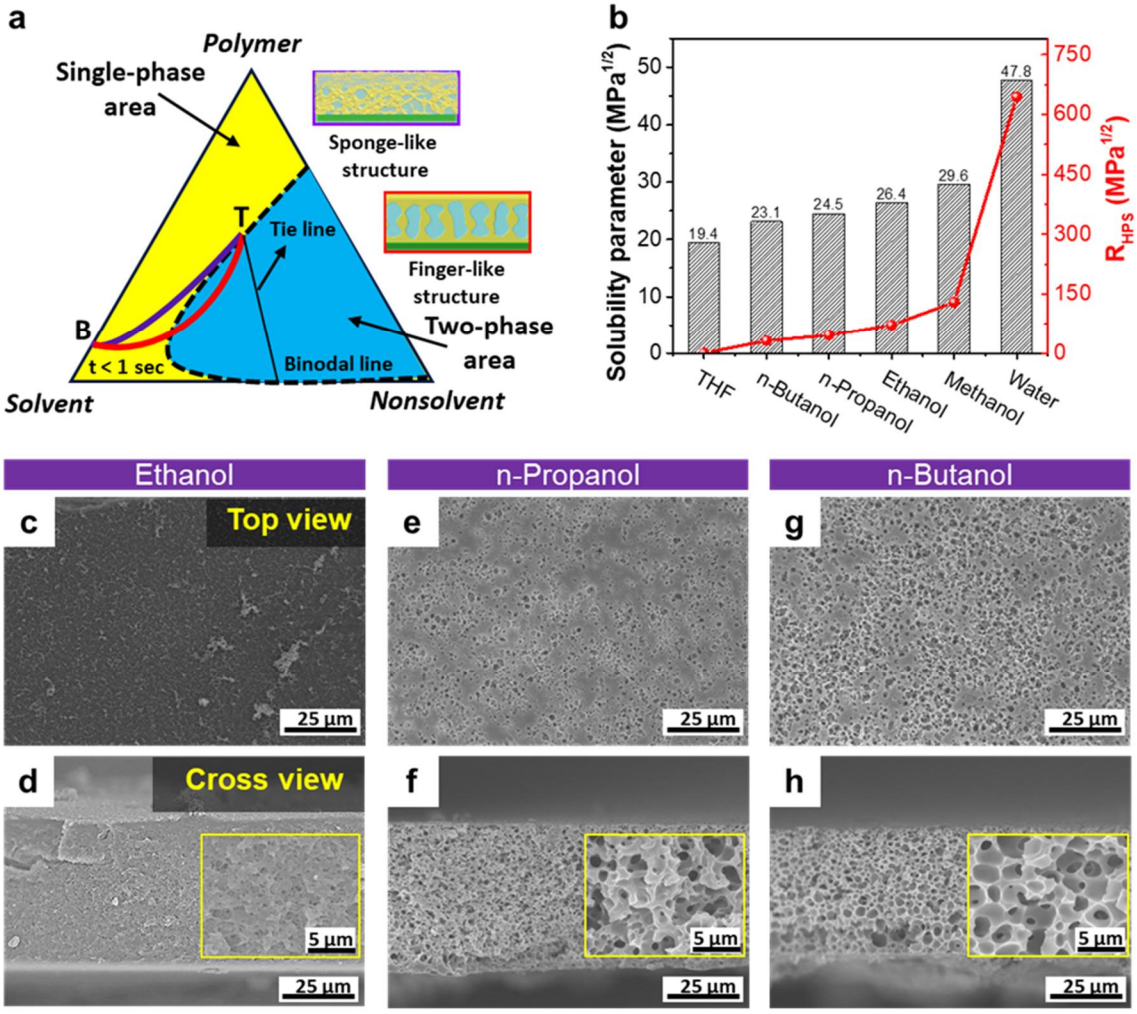

Figure 2-2. Schematic representation of ternary phase diagram and morphological characterization of SBN separator membranes fabricated by different nonsolvents. a) Composition paths of a cast film after immersion (t < 1s): purple line and red line induce spongelike and fingerlike structures, respectively. T and B represent top and bottom surfaces of the film, respectively. b) Solubility parameters of solvent, nonsolvents, and R_{HPS} between solvent and nonsolvent. SEM images of the SBN separator membrane fabricated by ethanol nonsolvent; c) top and d) cross view, n-propanol nonsolvent; e) top and f) cross view, and n-butanol nonsolvent; g) top and h) cross view. The inset shows magnified cross-sectional images.

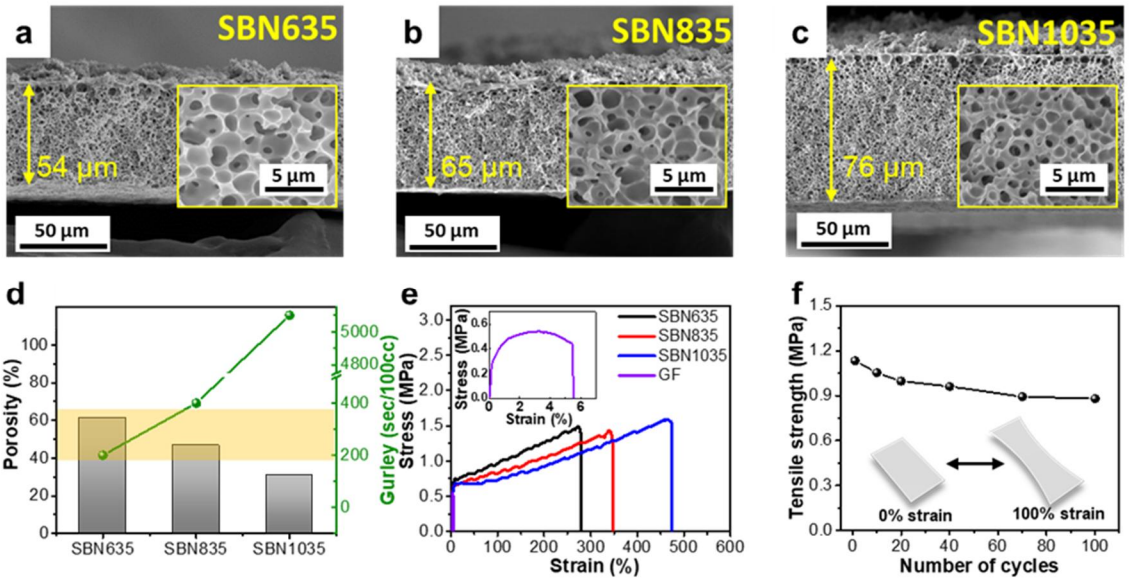

Figure 2-3. Morphological and mechanical characterization of the SBN separator membrane fabricated at different polymer concentrations. SEM images of the SBN separator membrane with different polymer concentrations of a) 6 wt%, b) 8 wt%, and c) 10 wt%, respectively. d) Changes in porosity and Gurley value of the SBN separator membrane with different polymer concentrations; highlighted range is the desirable porosity and Gurley values of separator for typical LIBs. e) Stretchability test of each SBN separator membrane. The inset shows the mechanical property of GF. f) The tensile strength of SBN635 separator membrane as a function of repeated strain cycles.

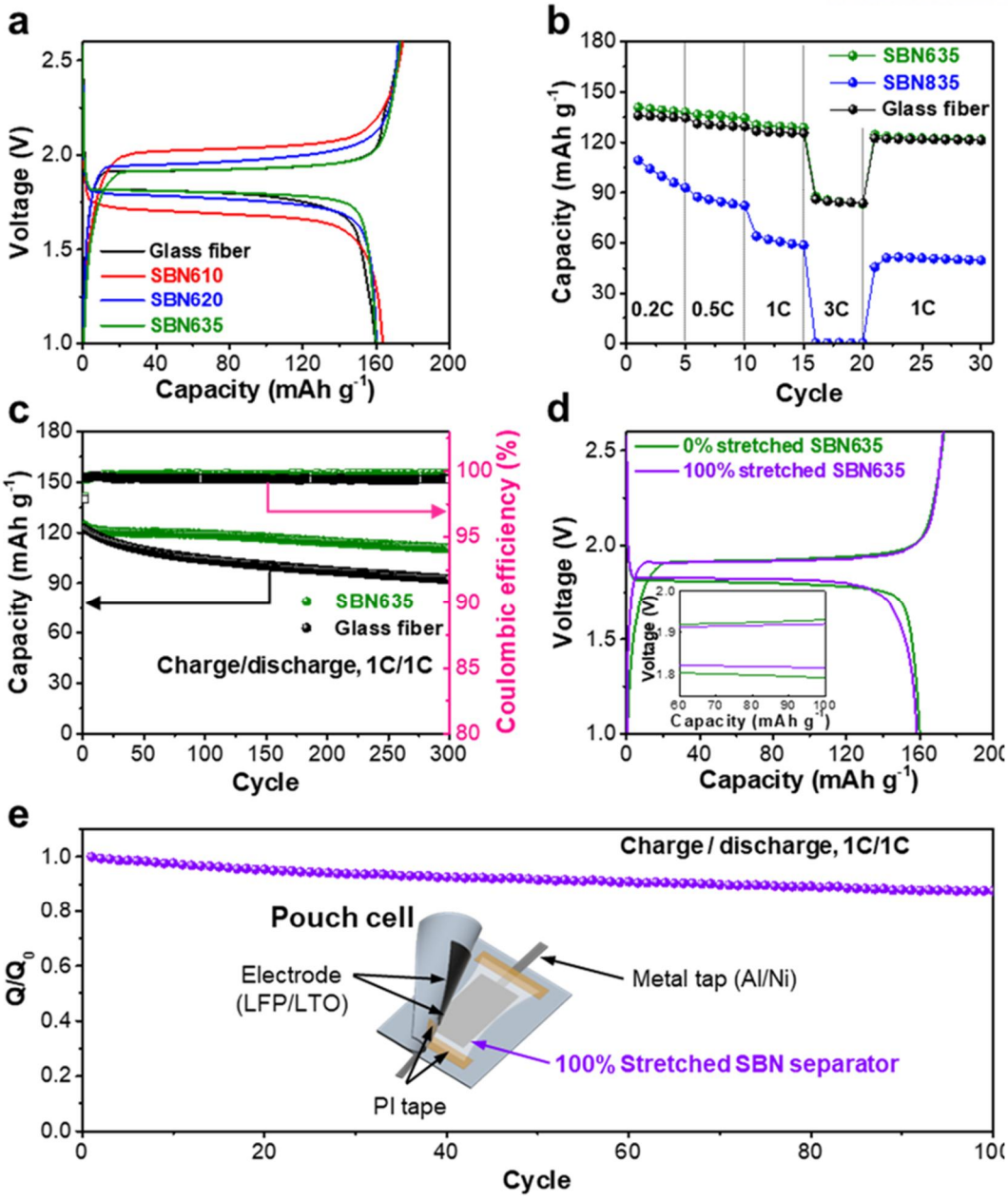

Figure 2-4. Electrochemical performances of the SBN separator membrane applied to LIBs based on organic electrolytes. a) Galvanotactic charge-discharge curves of full batteries with different oxygen plasma time versus a commercial GF separator at a rate of 0.1 C. b) Rate capability of the full batteries with various SBN separator membranes for 0.2-3 C. c) Long-term cycle performance and coulombic efficiency of the full batteries at a rate of 1 C for 300 cycles. d) Pre-cycles of SBN635 separator at unstretched and 100% stretched states at a rate of 0.1 C. The inset shows magnified charge-discharge curves of the full batteries. e) Relative discharge cycling performance of 100% stretched SBN-incorporated pouch-type full cell at a rate of 1 C over 100 cycles.

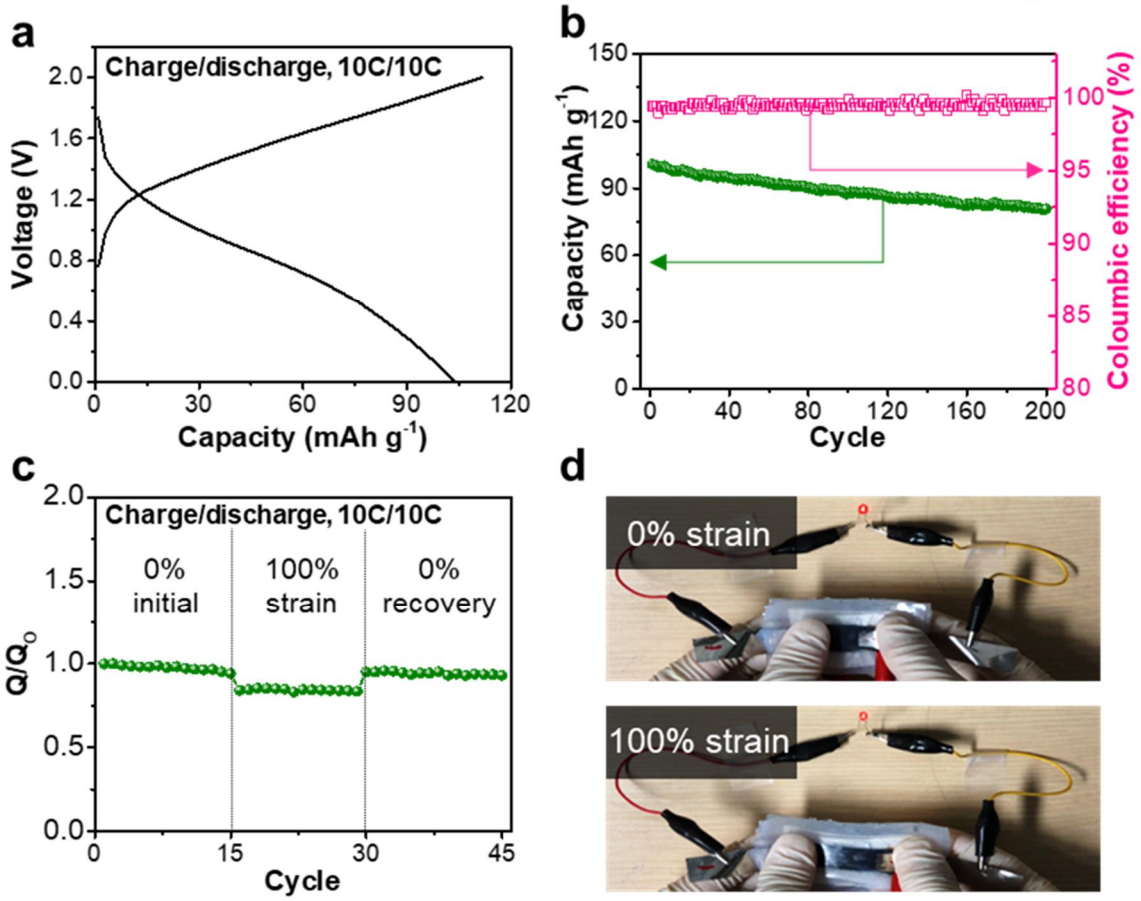

Figure 2-5. Electrochemical performances of stretchable ARLBs with the stretchable separator membrane. a) Charge-discharge profile of batteries at a rate of 10 C. b) Cycling performance and coulombic efficiency of the batteries at a rate of 10 C for 200 cycles. c) Cycle performance under strain and release. d) Photographs of a red LED powered by two stretchable ARLBs connected in series under 100% strain..

Material	Hansen parameters ($MPa^{1/2}$)				R_{HSP} ($MPa^{1/2}$)
	δ_d	δ_p	δ_h	δ_t	S-NS
SBS (7:3)				17.5 (ref)	
THF (Solvent)	16.8	5.7	8	19.4	
n-butanol	16	5.7	15.8	23.1	31.7
n-propanol	16	6.8	17.4	24.5	46.065
ethanol	15.8	8.8	19.4	26.4	71.785
methanol	15.1	12.3	22.3	29.6	129.805
water	15.6	16	42.3	47.8	644.17

Hansen solubility parameters

$\delta_t^2 = \delta_d^2 + \delta_p^2 + \delta_h^2$

δ_t = total Hildebrand parameter
δ_d = dispersion component
δ_p = polar component
δ_h = hydrogen bonding component

Hansen solubility parameter distance (between 1, 2)

$R_{HPS} = \sqrt{4(\delta_{d1} - \delta_{d2})^2 + (\delta_{p1} - \delta_{p2})^2 + (\delta_{h1} - \delta_{h2})^2}$

Table S2-1 Hansen's Solubility parameter and calculation of solubility parameter distance

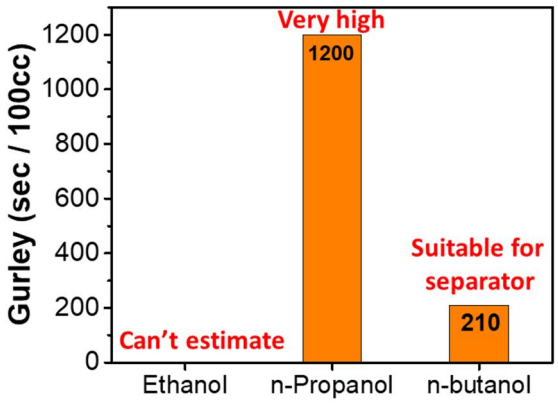

Figure S2-1. Gurley values of SBN separator fabricated by different nonsolvent.

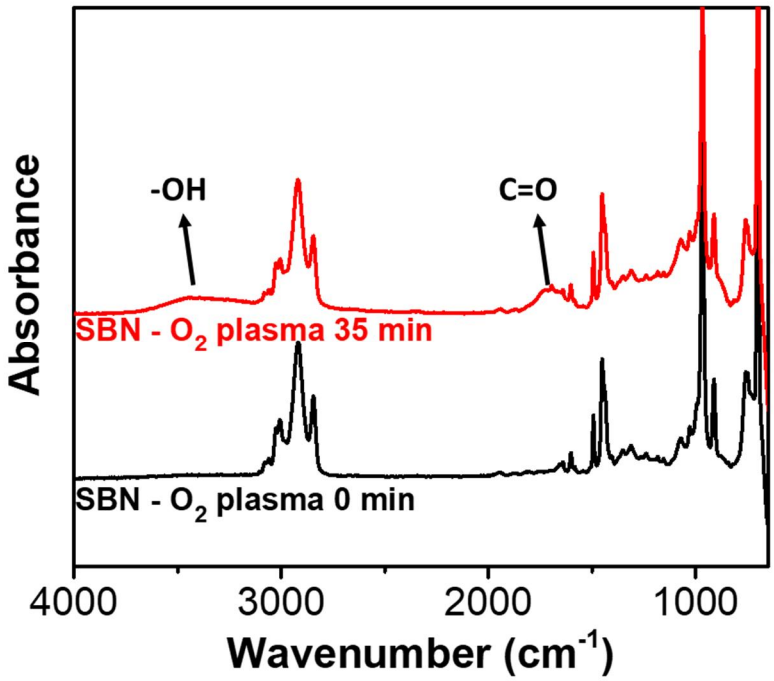

Figure S2-2. FT-IR spectra of oxygen plasma treated and untreated SBN separator.

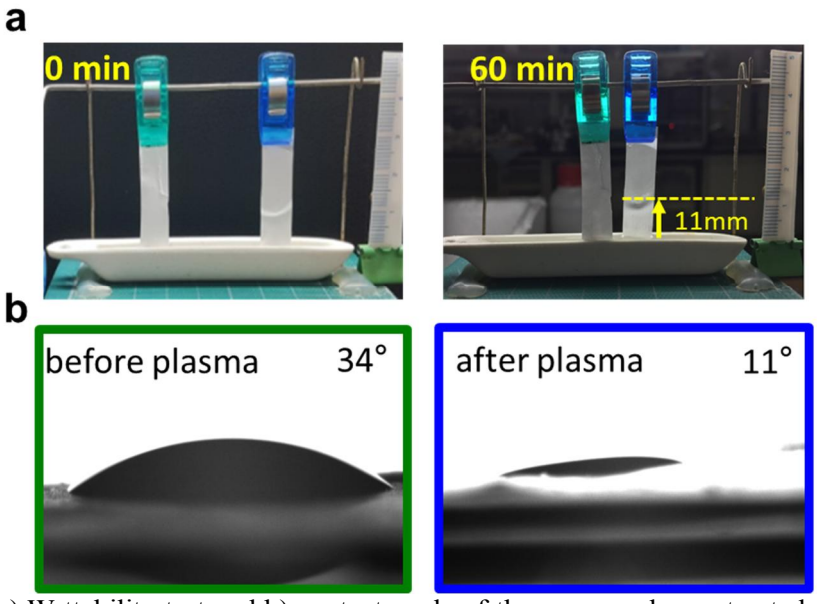

Figure S2-3. a) Wettability test and b) contact angle of the oxygen plasma treated (green color) and untreated SBN separator (blue color) to the EC/PC electrolyte.

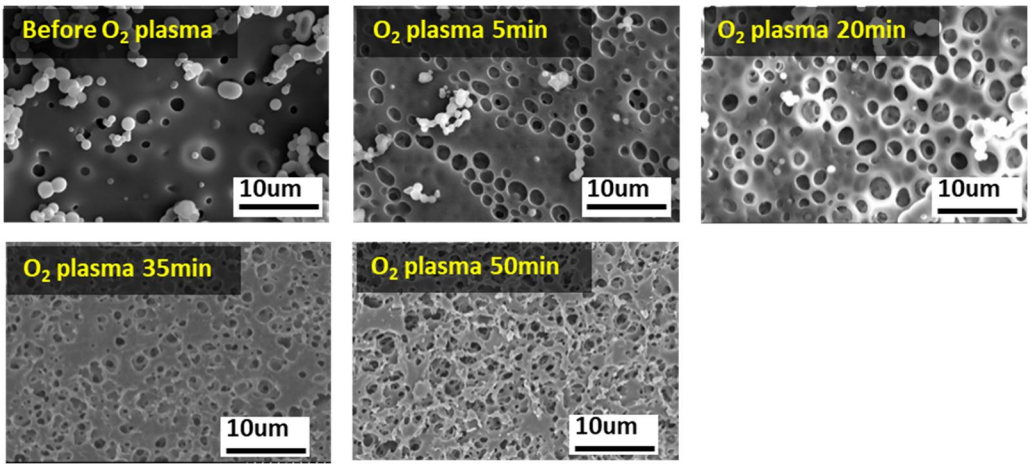

Figure S2-4. Top SEM images of the SBN6 separator as different O2 plasma treatment time.

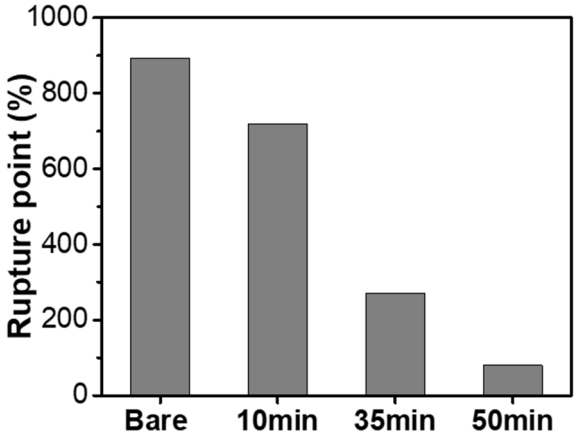

Figure S2-5. Stretchability test of SBN6 separator as different oxygen plasma treatment time.

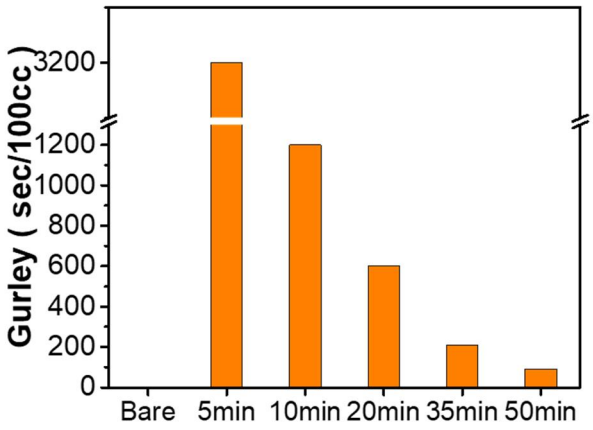

Figure S2-6. Gurley values of SBN6 separator as different oxygen plasma treatment time.

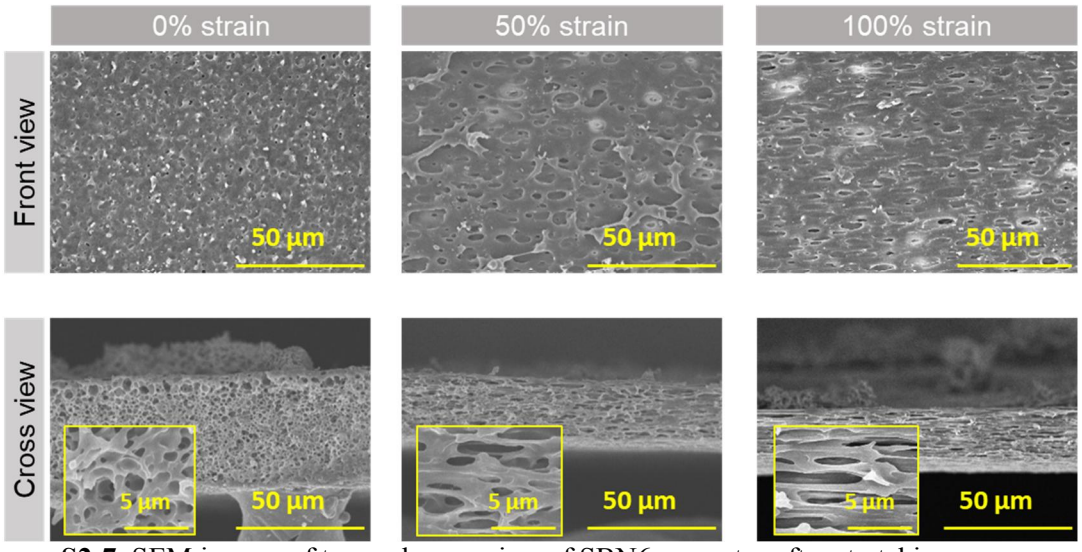

Figure S2-7. SEM images of top and cross view of SBN6 separator after stretching.

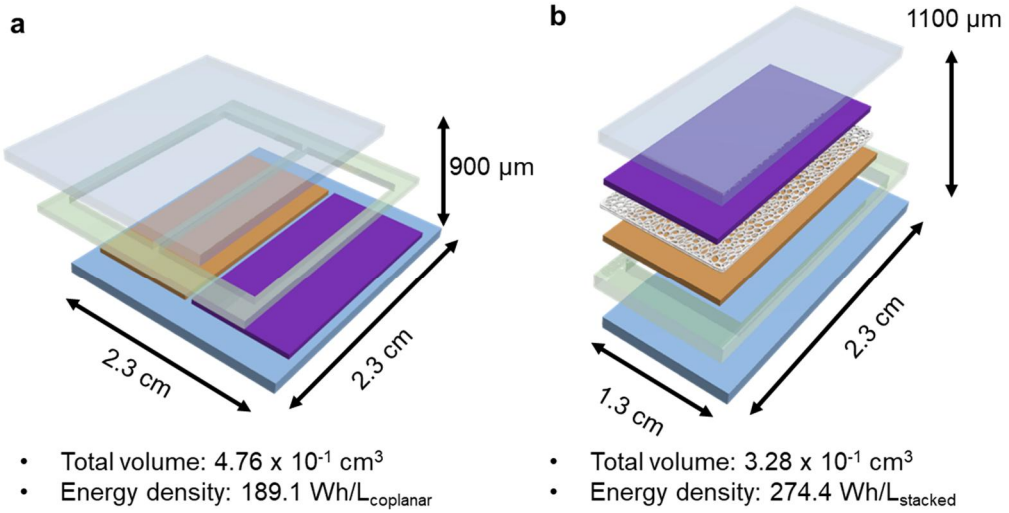

Figure S2-8. Comparison of total volume and energy denisty of a) coplanar and b) stacked configuration.

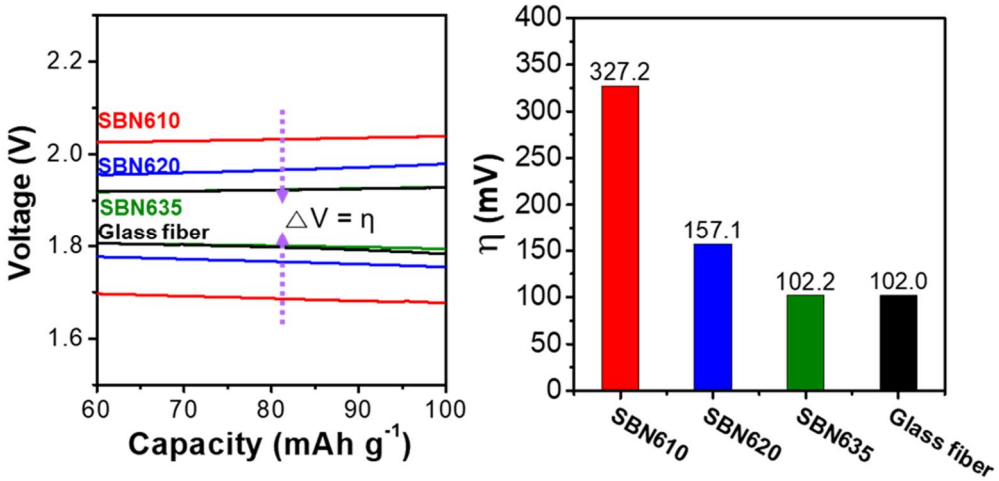

Figure S2-9. Overpotential of the full batteries with a various SBN separator membrane.

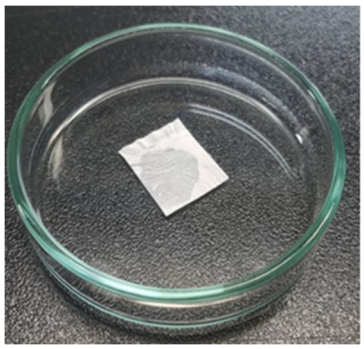

Figure S2-10. Digital photograph of SBN635 separator after drop the organic liquid electrolyte (1M LiPF6 in EC/PC).

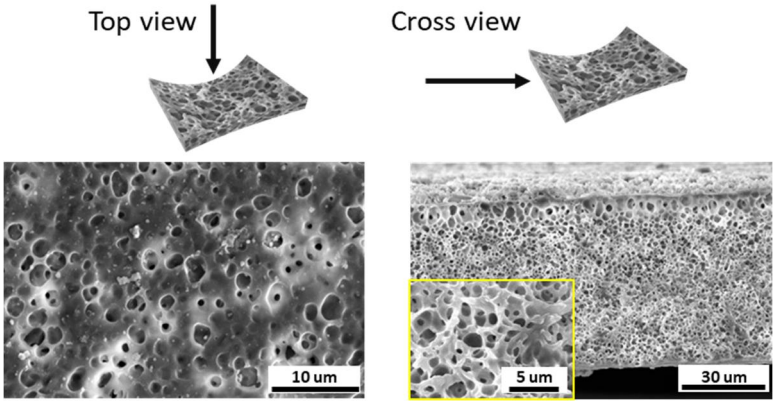

Figure S2-11. Top and cross SEM images of SBN635 separator after cycle.

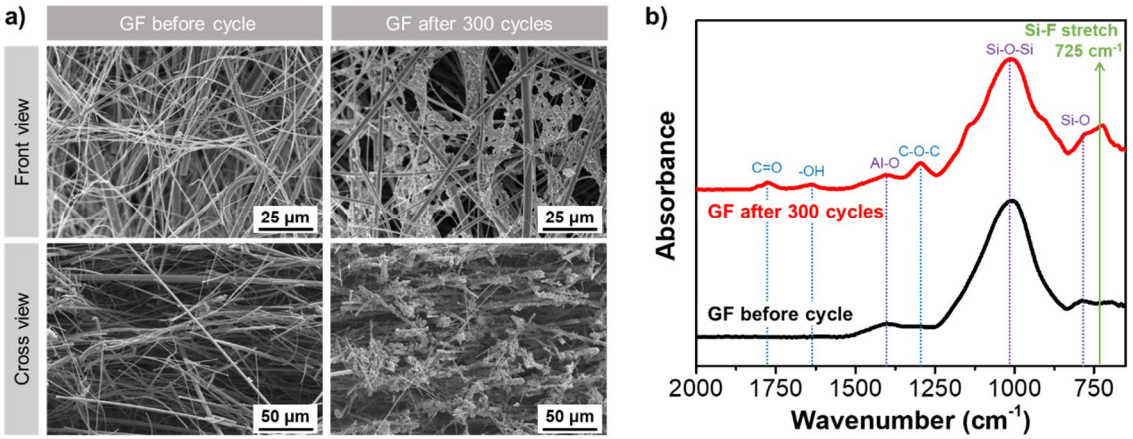

Figure S2-12. a) SEM images and b) FT-IR analysis of GF before and after 300 cycles.

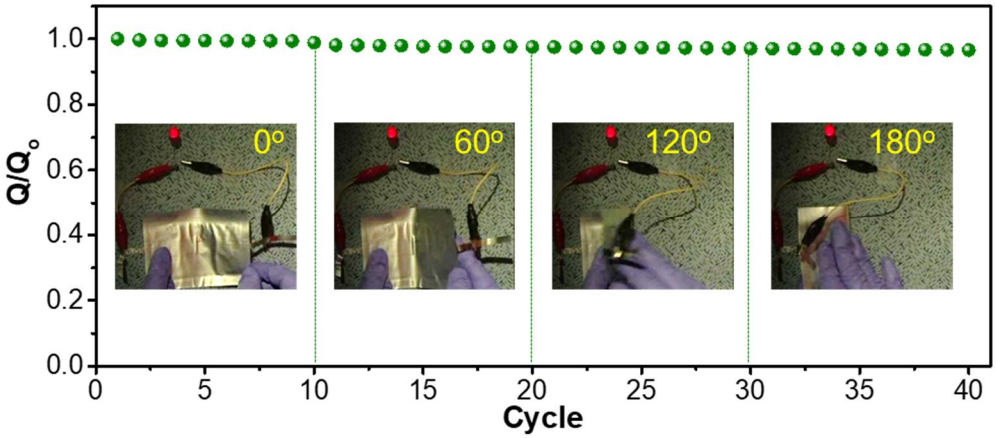

Figure S2-13. The relative discharge capacity of the organic electrolyte-based LIBs with SBN635 separator under various amount of folding.

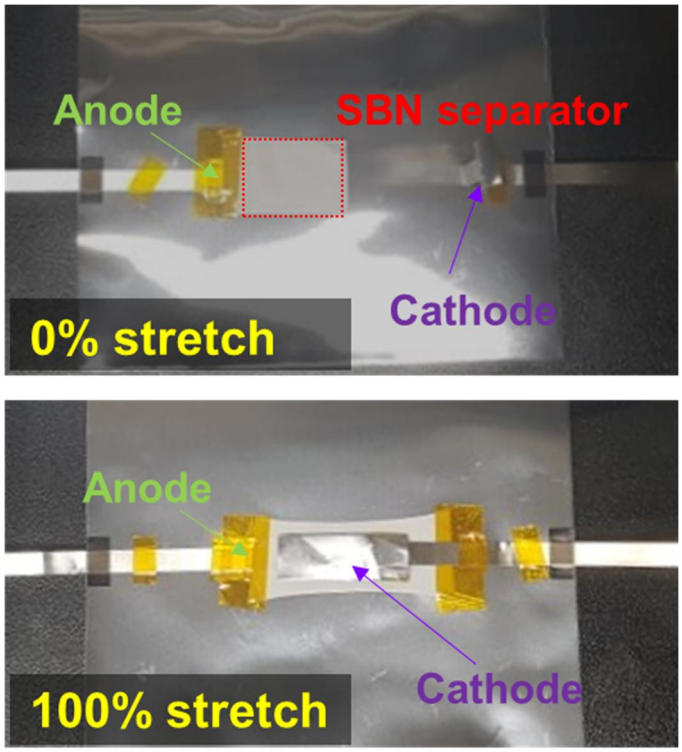

Figure S2-14. Digital photographs of the pouch type full-battery assembly with stretched SBN635 separator.

2.4 Conclusion

In summary, we fabricated the SBS block-copolymer based stretchable porous separator membrane for deformable power sources *via* a simple NIPS process which differs from the commonly adopted strategies for imparting stretchability to the separator. We demonstrated effective control of mechanical properties and porosity using the NIPS technology. The key parameters affecting final morphologies and critical properties of the separator membrane, such as a choice of nonsolvent, a concentration of polymer solution, and an oxygen plasma treatment time were controlled. A small R_{HSP} value, n-butanol as a nonsolvent with THF solvent, induced the well-defined separator membrane with a high porosity. Furthermore, an oxygen plasma treatment modified the surface of the SBN separator membrane to have proper porosity and to increase the electrolyte wettability. This series of procedure allowed the SBN separator membrane to be compatible with both deformable organic and aqueous electrolyte-based energy storage devices, resulting in its stable electrochemical performance without any problem related to internal short-circuit or mechanical failure even under 100% strain. This study is expected to accelerate developing technologies for energy storage devices and also provide a new class of manufacturing strategies for upcoming stretchable electronics.

2.5 Reference

[1] M. C. LeMieux, Z. Bao, *Nat. Nanotechnol.* **2008**, *3*, 585.

[2] J. A. Rogers, T. Someya, Y. G. Huang, *Science* **2010**, *327*, 1603.

[3] T. Sekitani, T. Someya, *Adv. Mater.* **2010**, *22*, 2228.

[4] K. Xie, B. Wei, *Adv. Mater.* **2014**, *26*, 3592.

[5] L. Li, Z. Wu, S. Yuan, X.-B. Zhang, *Energy Environ. Sci.* **2014**, *7*, 2101.

[6] W. Liu, M. S. Song, B. Kong, Y. Cui, *Adv. Mater.* **2017**, *29*,1603436

[7] D. J. Lipomi, B. C. K. Tee, M. Vosgueritchian, Z. Bao, *Adv. Mater.* **2011**, *23*, 1771.

[8] R. Kumar, J. Shin, L. Yin, J. M. You, Y. S. Meng, J. Wang, *Adv. Energy Mater.* **2017**, *7*, 1602096

[9] L. Hu, M. Pasta, F. La Mantia, L. Cui, S. Jeong, H. D. Deshazer, J. W. Choi, S. M. Han, Y. Cui, *Nano Lett.* **2010**, *10*, 708.

[10] C. Yan, X. Wang, M. Cui, J. Wang, W. Kang, C. Y. Foo, P. S. Lee, *Adv. Energy Mater.* **2014**, *4*, 1301396

[11] A. M. Zamarayeva, A. E. Ostfeld, M. Wang, J. K. Duey, I. Deckman, B. P. Lechêne, G. Davies, D. A. Steingart, A. C. Arias, *Sci. Adv.* **2017**, *3*, e1602051.

[12] Z. Song, T. Ma, R. Tang, Q. Cheng, X. Wang, D. Krishnaraju, R. Panat, C. K. Chan, H. Yu, H. Jiang, *Nat. Commun.* **2014**, *5*, 3140.

[13] S. Xu, Y. Zhang, J. Cho, J. Lee, X. Huang, L. Jia, J. A. Fan, Y. Su, J. Su, H. Zhang, *Nat. Commun.* **2013**, *4*, 1543.

[14] H. Lee, M. Yanilmaz, O. Toprakci, K. Fu, X. Zhang, *Energy Environ. Sci.* **2014**, *7*, 3857.

[15] H. Li, Y. Ding, H. Ha, Y. Shi, L. Peng, X. Zhang, C. J. Ellison, G. Yu, *Adv. Mater.* **2017**, *29*, 170898

[16] Z. Niu, H. Dong, B. Zhu, J. Li, H. H. Hng, W. Zhou, X. Chen, S. Xie, *Adv. Mater.* **2013**, *25*, 1058.

[17] J. Song, Y. Wang, C. C. Wan, *J. Power Sources* **1999**, *77*, 183.

[18] P. Hu, J. Chai, Y. Duan, Z. Liu, G. Cui, L. Chen, *J. Mater. Chem. A* **2016**, *4*, 10070.

[19] K. H. Choi, S. J. Cho, S. H. Kim, Y. H. Kwon, J. Y. Kim, S. Y. Lee, *Adv. Funct. Mater.* **2014**, *24*, 44.

[20] W. Liu, J. Chen, Z. Chen, K. Liu, G. Zhou, Y. Sun, M. S. Song, Z. Bao, Y. Cui, *Adv. Energy Mater.* **2017**, *7*, 1701076

[21] X. Li, T. Gu, B. Wei, *Nano Lett.* **2012**, *12*, 6366.

[22] J. Nam, Y. Huang, S. Agarwal, J. Lannutti, *J. Appl. Polym. Sci.* **2008**, *107*, 1547.

[23] M. Xie, J. Wang, X. Wang, M. Yin, C. Wang, D. Chao, X. Liu, *Macromol. Res*. **2016**, *24*, 965.

[24] S. Yoo, J.-H. Kim, M. Shin, H. Park, J.-H. Kim, S.-Y. Lee, S. Park, *Sci. Adv.* **2015**, *1*, e1500101.

[25] J. I. Kim, Y. Choi, K. Y. Chung, J. H. Park, *Adv. Funct. Mater.* **2017**, *27*, 1701768

[26] Z. Li, P. Zhang, H. Zhang, Y. Wu, X. Zhou, *Electrochem. Commun.* **2008**, *10*, 791.

[27] H. Zhang, H. Zhang, X. Li, Z. Mai, J. Zhang, *Energy Environ. Sci.* **2011**, *4*, 1676.

[28] A. Idris, A. Ismail, M. Noordin, S. Shilton, *J. Membr. Sci,* **2002**, *205*, 223.

[29] D. W. Wallace, C. Staudt-Bickel, W. J. Koros, *J. Membr. Sci,* **2006**, *278*, 92.

[30] E. Drioli, L. Giorno, E. Fontananova, *Comprehensive membrane science and engineering*, Elsevier, Amsterdam, Netherlands **2010**.

[31] J. Mulder, *Basic principles of membrane technology*, Kluwer Academic Publishers, London, UK **2012**.

[32] S. Simone, A. Figoli, A. Criscuoli, M. Carnevale, S. Alfadul, H. Al-Romaih, F. Al Shabouna, O. Al-Harbi, E. Drioli, *Desalination* **2014**, *344*, 28.

[33] N. N. Li, A. G. Fane, W. W. Ho, T. Matsuura, *Advanced membrane technology and applications*, Wiley, Hoboken, NJ, USA **2007**.

[34] H. Strathmann, K. Kock, *Desalination* **1977**, *21*, 241.

[35] P. J. Flory, *Principles of polymer chemistry*, Cornell University Press, Ithaca, NY, USA **1953**.

[36] B. Zhang, Q. Wang, J. Zhang, G. Ding, G. Xu, Z. Liu, G. Cui, *Nano Energy* **2014**, *10*,

277.

[37] V. Laninovic, *Desalination* **2005**, *186*, 39.

[38] C. M. Hansen, *Hansen solubility parameters: a user's handbook*, CRC press, Boca Raton, FL,USA **2007**.

[39] C. M. Hansen, *J. Paint Technol* **1967**, *39*, 105.

[40] M. Strobel, C. S. Lyons, K. Mittal, *Plasma surface modification of polymers: relevance to adhesion*, VSP, Utrecht, Netherlands **1994**.

[41] S. Y. Jin, J. Manuel, X. Zhao, W. H. Park, J.-H. Ahn, *J. Ind. Eng. Chem,* **2017**, *45*, 15.

[42] K. Abraham, *Electrochim. Acta* **1993**, *38*, 1233.

[43] Y. Mengüç, Y.-L. Park, H. Pei, D. Vogt, P. M. Aubin, E. Winchell, L. Fluke, L. Stirling, R. J. Wood, C. J. Walsh, *Int. J. Rob. Res*. **2014**, *33*, 1748.

[44] W. J. Song, J. Park, D. H. Kim, S. Bae, M. J. Kwak, M. Shin, S. Kim, S. Choi, J. H. Jang, T. J. Shin, *Adv. Energy Mater.* **2017**, 1702478

[45] S. Wiemers-Meyer, S. Jeremias, M. Winter, S. Nowak, *Electrochim. Acta* **2016**, *222*, 1267.

[46] C. Hwang, W. J. Song, J. G. Han, S. Bae, G. Song, N. S. Choi, S. Park, H. K. Song, *Adv. Mater.* **2017**, *30*, 1705445

Chapter . Metamorphosis of seaweeds into multitalented materials for energy storage applications

3.1 Introduction

Recently developed practical energy storage systems, such as portable consumer electronics, grid energy storage, and electric vehicles, require high-density and low-cost lithium-ion batteries (LIBs).[1–4] Although various factors determine energy density, cathode materials are a substantial capacity-dominant part; therefore, the effective utilization of cathode materials that exhibit high operating voltage and high reversible capacity has drawn extensive attention.[5–8] To date, transition metal oxide–based materials have been widely used as cathode materials for LIBs.[9–12] Mn-based spinel cathode materials, including $LiMn_2O_4$ (LMO) and $LiNi_{0.5}Mn_{1.5}O_4$ (LNMO), have attracted significant attention owing to their low cost, high operating voltage, and environment-friendly nature.[13,14]

Despite these beneficial features, Mn-based spinel cathode materials show very poor cycle retention, particularly at high temperature (> 55℃), because hydrofluoric acid (HF) formed by the hydrolysis of $LiPF_6$ in the electrolyte promotes the dissolution of the transition metal ions (Mn^{2+} and Ni^{2+}) from the cathode materials and induces parasitic side reactions with electrolytes.[15,16] To date, various strategies such as the surficial/structural engineering of cathode/anode materials, electrolyte additives, and functional separator membranes or binders have been reported to resolve this issue.[17–22] However, the majority of these methods only offer a fragmentary solution that is focused either stabilizing the cathode material, capturing the dissolved metal ions, or mitigating HF generation in the electrolyte. To circumvent the degradation of battery performance triggered by different concurrent reasons, the strategy that can address all issues at once is required.

A seaweed-derived agar consists of raw polysaccharides such as agarose and agaropectin, which are commonly employed in the food and biotechnology industries.[23,24] Nowadays, the utilization of polysaccharides for energy storage devices is a growing research interest because of their multi-functionality, low cost, light weight, environment-friendly characteristics. [25–28] In previous studies, agarose was regarded as a functional biomaterial for LIBs with the Mn-based cathodes owing to its transition metal ion–chelating ability.[21,22] However, the practical viability of the agarose to LIBs was restricted because of its relatively high price of about USD 600 kg^{-1}

compared with agar with a cheap price of USD 30–35 kg^{-1}.[29,30] Therefore, agar remains an attractive material in terms of cost and functionality, but its low mechanical property and various side groups make it difficult to be utilized as a separator membrane and binder.

In this study, we describe an effective approach for the utilization of agar as a functional separator membrane and binder for high-energy and cost-effective LIBs. We introduce 3-glycidoxypropyl trimethoxysilane (GPTMS) in agar as a surface modifier for the fabrication of a separator membrane via the nonsolvent-induced phase separation (NIPS) method, which is a promising approach for the fabrication of membranes with microporous structures.[31–34] The GPTMS-modified agar (G-Agar) separator membrane meets the major requirements for separator membranes in LIBs such as uniformly porous structure, high ionic conductivity, good wettability toward electrolytes, and excellent thermal stability. Moreover, agar is also simultaneously employed as a binder of Mn-based cathode materials to achieve a synergetic effect with the G-Agar separator membrane. LMO half cell results (95% after 100 cycles at a rate of 1 C at 60℃) show that the concurrent utilization of G-Agar separator membrane and agar binder exhibits beneficial synergic effects such as capturing the Mn^{2+} ions and the suppression of HF generation in $LiPF_6$-based electrolyte. For the practical level of batteries with high energy density, the agar binder and G-Agar separator membrane were introduced in a LNMO/graphite (LNMO/Gr) full cell system (10.9 mg cm^{-2}); a full cell with both the elements demonstrates relatively outstanding cycle retention performance (84.1% after 100 cycles at a rate of 1 C at 55℃) even at high-voltage operations under high temperatures. We believe that this study will provide insights into the feasible application of natural seaweeds into high-energy-density LIBs.

3.2 Experimental

Synthesis of GPTMS-Agar (G-Agar) solution

8 wt% Agar solution in DMSO (Sigma-Aldrich)/DMF (Sigma-Aldrich) (80:20, (w/w)) was reacted with different GPTMS (Sigma-Aldrich) amounts from 0.1 G-Agar (GPTMS/agar, 1:10 (w/w)) to the 1.0 G-Agar (GPTMS/Agar, 1:1 (w/w)) at 120 for 90 min for surface energy modification and cross-linking between the agar and GPTMS. The resulting G-Agar solution was employed for membrane fabrication without further purification.

Fabrication of agar and 0.5G-Agar separator membranes

The agar or G-Agar solution was cast on a flat silicon wafer substrate by using a doctor blade with a 300 μm gap. Thereafter, the film was immersed immediately in the ethanol nonsolvent bath for 12 h at room temperature. After the phase inversion process, the film was placed in a vacuum oven at 70 for 20 min to dry the solvent in the membrane.

Characterization

The tensile strength test was performed by a tensile strength machine (Petrol LAB DA-01). The morphology and physicochemical analysis of the separator membranes were investigated by SEM (FEI Verios 460), whereas the surface functional groups were examined using an FT-IR spectrometer (670-IR, Agilent). The water or electrolyte contact angle of the PE, agar, and G-Agar separator membrane were analyzed for hydrophobicity or wettability measurements to the liquid electrolyte by using a drop shape analyzer (DSA-100, KRÜSS GmbH). The air permeability of the separator membranes was measured via a Gurley densometer (4110N, Gurley), and their porosity was obtained by weighing before and after dipping in n-butanol for 30 min, in which the occupying volume was equivalent to the void volume of the separator:[36]

$$\text{Porosity}\ (\%) = \left(\frac{W-W_0}{\rho_L V_0}\right) \times 100 \quad (1)$$

where W and W_0 represent the weight of the separator after and before the absorption of n-butanol, respectively; V_0 is the geometric volume of the separator; and ρ_L is the density of n-butanol (0.81 g cm^{-3}). The wettability and absorption capability of the separator membrane for the liquid electrolyte was estimated by the measurement of the electrolyte absorption height after the

separator membrane was soaked for 1 hr. Thermal shrinkage was calculated by the measurement of the reduced dimension of the PE, agar, and 0.5G-Agar separator membranes before and after being heated in the hot oven at various temperature for 30 min. The time-of-flight secondary ion mass spectrometry (TOF-SIMS) spectrometer (ION-TOF GmbH, TOF SIMS 5) was used to analyze the surface components of separators soaked in electrolyte with 200 ppm water for 24 h; thereafter, the components were rinsed in dimethyl carbonate (DMC) and dried in an argon-filled glove box. TOF-SIMS analysis was performed in ultrahigh vacuum at a pressure less than 1.1×10^{-9} mbar. All detected secondary ions of F^-, $PO_2F_2^-$ showed a mass resolution of 5270, and 7900, respectively, and possessed negative polarity. A pulsed 25 keV Bi1 + (1pA) ion beam set in either the high current or burst alignment mode was applied for surface spectroscopy or image mapping at the typical analyzed area of 50 μm × 50 μm.

Electrochemical test

The LMO electrode was fabricated by casting a slurry composed of active material (LMO), conductive carbon (Super-P), and polymeric binder (PVDF, agar) dissolved in anhydrous NMP (Sigma-Aldrich) in a weight ratio of 85:10:5 on a piece of Al foil (15 μm). The residual NMP solvent was evaporated by placing the LMO electrode in a vacuum oven at 120 ℃ for 30 min. The areal specific capacity and loading level of the LMO cathode were 2.27 mA h cm^{-2} and 23.15 mg cm^{-2}, respectively. Any traces of water physically bound to the cathode and anode were minimized as the LMO electrode dried at 110℃ for 12 h under vacuum before cell assembly. Moreover, the 2032 coin-type half cells were assembled in an argon-filled glove box (with moisture and oxygen levels of less than 1 ppm). The LMO/Li metal half cells were galvanostatically cycled between 4.3–3.0 V using a computer-controlled battery measurement system (WonATech WBCS 3000); their formation and subsequent cycling were performed at a rate of C/10 and 1 C in a constant-temperature drying oven at 25℃ and 60℃. The cell resistance of the LMO half cell was obtained by measuring the electrochemical impedance spectroscopy (EIS) in the 10^{-2}–10^{-6} Hz frequency range. LNMO cathode was fabricated by casting a slurry composed of 85 wt% active material, 10 wt% Super-P, and 5 wt% PVDF binder; dissolving it in anhydrous NMP on a piece of Al foil (15 μm); subsequently drying it in a convection oven at 120℃ for 30 min. The areal specific capacity and loading level of the LNMO cathode were 1.34 mA h cm^{-2} and 10.9 mg cm^{-2}, respectively. Also, the graphite anode was prepared by casting a slurry composed of 96 wt% active material, 1 wt% Super-P, 3 wt% binder (1.5 wt% styrene-butadiene rubber (SBR, BM-400B, Zeo

n), and 1.5 wt% carboxyl methylcellulose (CMC, MAC500LC, Nippon paper group) bin der; dissolving it in distilled water on a piece of Cu foil (18 μm); and drying it in a c onvection oven at 80℃ for 30 min. Dried LNMO cathode and graphite anode were pres sed using a rolling mill, and a full cell was designed with a N/P ratio of 1.15. Any tra ces of water physically bound to the cathode and anode were minimized by drying both the LNMO cathode and graphite anode under vacuum at 110℃ for 12 h before cell as sembly. 1M $LiPF_6$ dissolved in FEC (Fluoroethylene carbonate, Enchem Co., Ltd) : EM C (Ethylmethyl carbonate, Soulbrain Co., Ltd.) : PFE (partially fluorinated ether based o n a mixture of 1,1,1,2,2,3,3,4,4-nonafluoro-4-methoxybutane and 2-(difluoro(methoxy)meth yl)-1,1,1,2,3,3,3-heptafluoropropane, Sigma Aldrich) (1:6:3, v/v/v) was prepared as the ba seline electrolyte of the full cell and later treated with calcium hydride (CaH_2, Sigma A ldrich) for water molecule elimination to prevent hydrolysis of $LiPF_6$ salt. The 2032 coi n-type full cells were assembled in an argon-filled glove box (with moisture and oxygen levels of less than 1 ppm), and the LNMO/graphite full cells were galvanostatically cy cled between 4.9–3.5 V via a computer-controlled battery measurement system (WonATe ch WBCS 3000); the formation and subsequent cycling were performed at a rate of C/1 0 and 1 C in a constant-temperature drying oven at 25℃ and 55℃, respectively.

3.3 Results and discussion

Figure 3-1a shows the fabrication process of the G-Agar separator membrane. Initially, agar powder was dissolved in a solvent mixture of dimethyl sulfoxide (DMSO) and dimethylformamide (DMF). In our previous study, we modified a block copolymer with GPTMS to adjust the surface chemistry; this approach induced a different phase separation behavior during the NIPS process and served as the HF scavenging unit.[19] Similarly, the GPTMS can play a vital role in modifying the surface energy of the agar and in improving its flexibility. The silane group can simultaneously react with the hydroxyl group in the agar and in the diol formed by ring opening of the epoxide, whereas self-polymerization of GPTMS produces a more elastic G-Agar. To understand the chemical reaction between GTPMS and agar, we performed the Fourier-transform infrared spectroscopy (FT-IR) analysis (**Figure S3-1** and **Table S3-1**). An intensity of Si–O–C peak (1070 cm^{-1}) clearly increased compared with ether peak in the polysaccharides (C–O–C, 1050 cm^{-1}) owing to the reaction between hydrolyzed GPTMS and agar. Furthermore, a peak related to siloxane bond (Si–O–Si, 1015 cm^{-1}) was observed from the crosslinked silicone. The as-prepared G-Agar solution was cast into a film by a doctor blade onto a flat substrate. The film was then immersed in the ethanol nonsolvent bath where porous morphologies in the G-Agar film were developed by a demixing process (liquid–liquid separation) of the NIPS method. After enough demixing, it was dried in a vacuum chamber at 70 for 20 min to yield a free-standing G-Agar separator membrane. The separator membrane had a 3D porous structure, as shown in the scanning electron microscopy (SEM) analysis **(Figure 3-1b–d)**. This series of manufacturing processes is applicable in a large-scale fabrication because of its simplicity and scalability (**Figure S3-2**).

In the NIPS process, the thermodynamic interactions and kinetics of the polymer chains during phase separation influence the final porous structure of the membrane.[34] The interactions between polymer, solvent, and nonsolvent mainly decide the type of membrane. In general, two membrane types, namely, sponge- and finger-like membranes, are determined by the solvent–nonsolvent exchange rate upon immersion in the nonsolvent bath. A fast solvent–nonsolvent exchange causes an instantaneous demixing that forms the finger-like structure membrane with macrovoids, whereas a slow exchange does not demix instantly and delays demixing, thus leading to a sponge-like morphology with small pores.[35]

In this study, the porous structure was determined by the amount of surface modifier, namely, GPTMS, incorporated in the natural polymer agar (i.e., different amounts resulted in different demixing rates and final pore structures). The agar possessed a hydrophilic nature and had good

affinity with ethanol nonsolvent, thus indicating that macrovoids in the final membrane developed via fast solvent–nonsolvent exchange in the nonsolvent-based ethanol bath (**Figure 3-2a**). Although the large macrovoids in the separator membrane enable a fast Li-ion transport, they may weaken mechanical strength of the membrane and cause a self-discharging issue,[36] thus necessitating us to introduce hydrophobic GPTMS groups into the agar polymer structure to manipulate its hydrophilic nature. To clarify the effect of GPTMS modification, we precisely adjusted the amount of GPTMS from 0.1G-Agar (GPTMS/agar = 1/10 (w/w)) to 1.0G-Agar (GPTMS/agar = 1/1 (w/w)). At higher GPTMS amount, the hydrophilic agar transformed into a hydrophobic G-Agar. In the ethanol nonsolvent bath, the low affinity between ethanol nonsolvent and G-Agar reduces the solvent–nonsolvent exchange rate; therefore, macrovoids in the membrane gradually decreased toward a symmetric dense membrane (**Figure 3-2c, e**). Moreover, the surface pore size of the G-Agar membrane dramatically decreased from micrometer size to a nanometer size (**Figure 3-2d, f**). To elucidate the changes in the surface energy and porosity of the G-Agar separator membrane, we conducted water contact angle and porosity analysis (**Figure 3-2g**). The porosity of the agar separator membranes decreased from 81% to 40%, whereas the water contact angle clearly increased from 16° to 60° because of increased GPTMS modification. These results demonstrate that the GPTMS modification affected the surface energy of agar and eventually changed the final membrane structure. A highly modified agar of over 0.5G-Agar using GPTMS heavily produced cross-linked bonds within the polymer structure and made the solution very viscous (**Figure S3-3**). Therefore, we selected 0.5G-Agar, which has favorable viscosity, for the casting process of NIPS because it was characterized by a symmetric porous structure without macrovoids.

To further demonstrate the advantages of a 0.5G-Agar (GPTMS/agar = 1/2 (w/w)) separator membrane for practical LIB applications, we compared the different properties of agar, 0.5G-Agar, and commercially available polyethylene (PE) separator membranes. We performed a tensile strength test to investigate the mechanical properties of each material under the same conditions as a function of the amount of GPTMS modification (**Figure 3-3a**). The agar separator membrane without GPTMS modification showed low tensile strength, elongation break of approximately 4.5% due to many macrovoids, and inherently weak physical properties of natural biomaterials.[24] By contrast, the 0.5G-Agar separator membrane exhibited a tensile strength that is twice that of agar, and this property was ascribed to the reduced macrovoids in the separator membrane and increased crosslinking between GPTMS and agar. These results demonstrate that the GPTMS modification could enhance the mechanical strength of agar polymer.

We also performed Gurley analysis for the estimation of air passing time via a defined area of

the various separator membranes under a specified pressure.[36] A low Gurley value indicates fast air penetration through large pores of macrovoids or well-interconnected pores. On the contrary, a high Gurley value indicates that air is having difficulty passing through the membrane via the dense structure with small pores, it exhibits high Gurley values. For these reasons, the Gurley values and porosity are always in a trade-off relationship (**Figure 3-3b and Figure 3-2g**). The measured Gurley value of the agar separator membrane was approximately 17 s owing to the presence of macrovoids; the 0.5G-Agar separator membrane showed a higher Gurley value of 105 s, and the PE separator membrane exhibited the highest Gurley value of 280 s. The results show that although the separator membrane with a low Gurley value (or high porosity) helps facilitate the migration of Li-ions through the porous structure, it simultaneously causes an internal short circuit via the penetration of Li dendrite through the macrovoids, as well as a self-discharge via an electrical leakage.[36] Therefore, the 0.5G-Agar separator membrane was suitable for providing fast charge–discharge performance and adequate battery stability.

We measured the wettability of the agar, 0.5G-Agar, and PE separator membranes toward carbonate-based electrolyte (1 M $LiPF_6$ dissolved in ethylene carbonate (EC)/diethyl carbonate (DEC), 1/1 (v/v)). Ion transport properties of the separator membrane are mostly governed by the wettability to the electrolytes.[37] Additionally, the high uptake ability of the electrolytes of the separator membrane is essential for high ionic conductivity.[38] **Figure 3-3c** shows the PE separator membrane had poor wettability toward the 1 M $LiPF_6$ in EC/DEC (v/v, 1/1) electrolytes because of its low surface energy and nonpolar nature, which interrupts the facile ion transport between the cathode and anode.[39] By contrast, the agar and 0.5G-Agar separator membrane exhibited excellent wettability to the same electrolytes; in particular, the 0.5G-Agar separator membrane showed the highest uptake ability after the immersion in the liquid electrolyte for 1 h. Furthermore, its electrolyte contact angle was the lowest among the membranes (**Figure S4**). Thus, it is clear that the introduction of GPTMS as a surface energy modifier enhanced the affinity to the carbonate-based electrolyte; thus, we expected the 0.5G-Agar separator membrane to show high ionic conductivity, which was three times higher than that of the PE separator membrane (**Figure 3-3d**).

Finally, we placed the three materials in a hot vacuum oven to measure their thermal shrinkage property, which is an important function of a LIB separator membrane for the prevention of electrical and physical contact between the two electrodes because it provides a Li-ion conduction pathway. Commercial polyolefin-based separators easily collapse their porous structure at temperatures above melting point and eventually cause an internal short circuit as the cathode and anode comes into contact.[40] **Figure 3-3e** shows the thermal shrinkages of PE, agar, and 0.5G-

Agar separator membranes at various temperatures for 30 min. The thermal shrinkage of the PE separator membrane gradually increased from 11% to 94% as the temperature increased from 100 to 140□; after being stored at 140 for 30 min, its pores eventually collapsed (**Figure S3-5a**) with greatly reduced dimension (**Figure S3-6**). The agar separator membrane showed relatively low but still insufficient thermal shrinkage to prevent an internal short circuit by the electrodes. In the SEM analysis (**Figure S3-5b**), the pores of the agar separator membrane partially shrunk after thermal treatment at 140 for 30 min. Moreover, the 0.5G-Agar separator membrane exhibited the lowest thermal shrinkage of approximately 1% even at elevated temperatures of 140 owing to cross-linked GPTMS on the agar. **Figure S3-5c** shows the SEM images of the 0.5G-Agar separator membrane before and after thermal treatment. The porous structure was maintained without noticeable changes, thus preventing an internal short circuit even with the undesired over-charge of LIBs.

To explore the effect of the G-Agar separator membrane and the agar binder on the LIB system, we prepared a half cell consisting of an LMO cathode and lithium metal anode with 1 M $LiPF_6$ in EC/DEC (v/v, 1/1) electrolyte. The LMO mass loading was 23.15 mg cm^{-2} (corresponding areal capacity of 2.27 mA h cm^{-2}). **Figure 3-4a** shows the half cells with different separator membranes/binders (PE/PVDF binder, PE/agar binder, agar/agar binder, 0.5G-Agar/agar binder) displayed similar galvanostatic charge/discharge curves at a 0.1 C rate in a voltage range of 3.0–4.3 V (*vs.* Li/Li^+). Furthermore, the similar initial Coulombic efficiencies of almost 99.5% were obtained for all half cells. To further investigate the electrochemical stability of as-prepared separator membranes in LIB systems, we conducted cyclic voltammetry (CV) characterization under a 0–5 V voltage range at 2 mV sec^{-1} **(Figure S3-7)**. The CV curves of the 0.5G-Agar separator membrane did not indicate any appreciable reactions, except for the electrolyte decomposition peaks, thus indicating its applicability for wide voltage range.

Figure 3-4b presents the rate performance of the half cells with the PE/PVDF binder, PE/agar binder, agar/agar binder, and 0.5G-Agar/agar binder at various rates from 0.5 C (53 mA g^{-1}) to 10 C (1060 mA g^{-1}) at room temperature. The 10 C rate capability of the PE/agar binder was improved with 44% of the initial discharge capacity (48 mA h g^{-1}), and only 8% of the initial discharge capacity was maintained (8.5 mA h g^{-1}) for the PE/PVDF binder; this phenomenon could be attributable to the fast Li-ion transport within the cathode due to the ability of agar binder that facilitate the electrolyte penetration into the cathode and helps the uniform electrolyte distribution. It is indicative that the agar binder is promising candidate as a binder for LIBs with Mn-based cathodes. Furthermore, compared with PE/agar binder cell, the agar/agar binder and 0.5G-Agar/agar binder cell, which differ only with regard to their separators, showed the

capability of delivering a discharge capacity of 78 mA h g^{-1} at a 10 C rate (73% at 10 C/0.5 C).

To elucidate the beneficial effects of the G-Agar separator membrane and agar binder in a battery system at 60 , we conducted the cycle test of LMO half cells (areal capacity of 2.27 mA h cm^{-2}) at 1 C/1 C (**Figure 3-4c**). The LMO cathode material consistently exhibited poor capacity retention at 60 because of the Mn^{2+} dissolution behavior by the HF attack in the $LiPF_6$-based electrolytes.[15,16] The HF directly attacked the cathode surface, thus resulting in Mn^{2+} dissolution into the electrolyte and the Mn contamination of the anode surface and increasing cell impedance.[41] Therefore, the half cell with a PE/PVDF binder suffered from severe capacity fading during cycling (capacity retention of only 35% after 30 cycles). By contrast, the agar binder enhanced capacity retention to 68% after 30 cycles, thus indicating that ether and hydroxyl groups in agar-based materials (binder and separator membrane) effectively chelated Mn^{2+} ions within the cathode (**Figure S3-8**) and the lone pair electrons of O atom in the agar effectively stabilized highly reactive PF_5, which is attributable to the HF generation by the undesirable reaction of PF_5 (g) + H_2O (l) → POF_3 (g) + 2HF (g).[21,22] The detailed mechanism of the stabilizing the PF_5 by the agar will be described later. Although the agar binder contributed to a slight improvement of cycling performance, its capacity decay still appeared because the amount of binder in the cathode is not enough to scavenge the PF_5 (approximately 5 wt% of the slurry). However, the increased amount of the agar binder lowered the energy density; therefore, agar binder was used together with the agar-based separator membranes (Agar, 0.5G-Agar) to maximize the beneficial effects. The agar/agar binder and 0.5G-Agar/agar binder cell astoundingly enhanced cycling stability; in particular, the 0.5G-Agar/agar binder cell of 96% presented better capacity retention than the Agar/agar binder cell (91%). The origin of this drastic improvement in capacity retention was examined by SEM measurement and energy dispersive spectroscopy (EDS) analysis of separator membranes after 100 cycles (**Figure S3-9**). As shown in the SEM images, the by-products were observed across the 0.5G-Agar separator membrane surface (**Figure S3-9a**), whereas the PE separator membrane had a relatively clean surface. The EDS results revealed that a high amount of Mn and F elements are chelated by agar and 0.5G-Agar separator membranes (**Figure S3-9b**). The higher amount of MnF_2, which is known to be generated via the undesired reaction between dissolved Mn^{2+} ions and a HF in the electrolyte, was detected for the 0.5G-Agar separator membrane.[42] From these results, the excellent cycling stability of the 0.5G-Agar/agar binder cell without noticeable capacity decay was attributable to the following synergetic effects: ( ) the high Mn^{2+} chelating ability of the agar, ( ) the inhibition of HF generation by Lewis acid, PF_5 scavenging ability of the lone pair electrons acting as a Lewis base in the agar, (iii) the improved separator membrane properties of the G-Agar, such as a uniformly porous structure, good wettability toward electrolyte, and high ionic conductivity.

To further demonstrate the role of the 0.5G-Agar separator membrane for the Mn-based cathode materials, we investigated the impedance of the LMO half cells with PE/PVDF binder, PE/agar binder, agar/agar binder, and 0.5G-Agar/agar binder after 100 cycles at 60 by means of the electrochemical impedance spectroscopy (EIS) measurements (**Figure 3-4d**). The Nyquist plots shows the contribution to the cell impedance from three components including the electrolyte resistance (R_s), impedance associated with the interfacial layer on anode electrodes (R_{SEI}), resistance for the faradaic charge transfer reaction at low frequency (R_{ct}), and Warburg diffusional impedance (Z_W). **Figure 3-4d** and **Table S3-2** shows that the R_{SEI} and R_{ct} of the 0.5G-Agar/agar binder cell incurred the lowest resistance (7 and 9 Ω, respectively) compared with the agar/agar binder (50 and 25 Ω), PE/agar binder (127 and 100 Ω), and PE/PVDF binder (215 and 135 Ω); this finding could be associated with the reduction of resistive LiF that can be produced by HF, the alleviation of HF-triggered solvent decomposition, and the inhibition of Mn^{2+} dissolution/deposition.

The major cause of the Mn^{2+} dissolution from Mn-based spinel cathode materials is the HF, which is formed by the hydrolysis of PF_5.[15] Therefore, blocking the undesirable reaction between PF_5 and water would prevent the generation of the HF. On a basis of previous reports, lone pair electrons in P, O, and N atoms were able to effectively form a complex with PF_5.[43] We expected that the agar-based material would have a PF_5 stabilizing effect because it had a large number of O atoms. To confirm the PF_5 stabilization function of the Agar-based separator membranes, the surface components of separators soaked in the electrolyte with 200 ppm water for 24 h were identified by a time-of-flight secondary ion mass spectrometry (TOF-SIMS) analysis (**Figure 3-4e**). Unlike the surface of the PE separator membrane, the signal associated with F^- and $PO_2F_2^-$ were greatly reduced on the surface of agar separator membranes. It is clear that agar-based separator membranes were very effective to stabilize PF_5, which suppressed the formation of $PO_2F_2^-$ and F^- by PF_5 hydrolysis.

To verify the effect of the 0.5G-Agar separator membrane/agar binder system on improving the electrochemical performance of full cells, we assembled graphite/LNMO full cells with high areal capacity (1.34 mA h cm^{-2}) (**Figure 3-5a**). The first galvanostatic charge–discharge voltage profiles of full cells with a PE/PVDF binder, agar/agar binder, and 0.5G-Agar/agar binder in the potential window of 3.5–5.0 V (*vs.* Li/Li^+) at a 0.1 C rate (**Figure 3-5b**). The overpotential of the full cell with agar/agar binder and 0.5G-Agar/agar binder significantly decreased compared with that of the full cell with a PE/PVDF binder (**Figure S3-10**). These results reveal that the agar/agar binder and 0.5G-Agar/agar binder enhance the electrolyte wettability and ionic conductivity, and they allow facile Li ion transport on charge and discharge (**Figure 3-3c** and **3-3e**).

Moreover, full cells with agar-based separator membranes/agar binder showed a substantial improvement in the cycling performance (**Figure 3-5c**). Remarkably, full cell with 0.5G-Agar/agar binder demonstrated the drastically improved cycle retention at high temperature (84.1 % after 100 cycles at 55). **Figure 3-5d** presents the high temperature storage performance of LNMO/graphite full cells of PE/PVDF binder, agar/agar binder, and 0.5G-Agar/agar binder. Open-circuit voltage (OCV) of fully charged full cell of the PE/PVDF binder sharply dropped during stored for 10 h at 55 . Unlike the full cell of the PE/PVDF binder, LNMO/graphite full cells with agar/agar binder and the 0.5G-Agar/agar binder favorably maintained the voltages without severe OCV drop for 80 h at 55 . The agar-based separator membrane and binder could effectively inhibit the transition metal ion (Mn^{2+} and Ni^{2+}) dissolution from the LNMO cathode the transition metal ion deposition on the graphite anode surface when stored at 55 and thus achieve improved high temperature storage performance. As a result, it is noteworthy that the full cells with 0.5G-Agar/agar binder can deliver a high areal energy density as well as show marvelous cycling stability rather than the previously reported Mn-based full cell system at high temperature (**Figure 3-5e**). Lastly, to further utilize the 0.5G-Agar/agar binder for the high-performance LIBs with a practical level of energy density (8.46 mW h cm^{-2}), we assembled the LNMO/graphite full cells with an immense areal capacity of 1.9 mA h cm^{-2}, resulting in stable capacity retention of 65% after 100 cycles at 60 compared with full cell with PE/PVDF binder (**Figure S3-11** and **S3-12**).

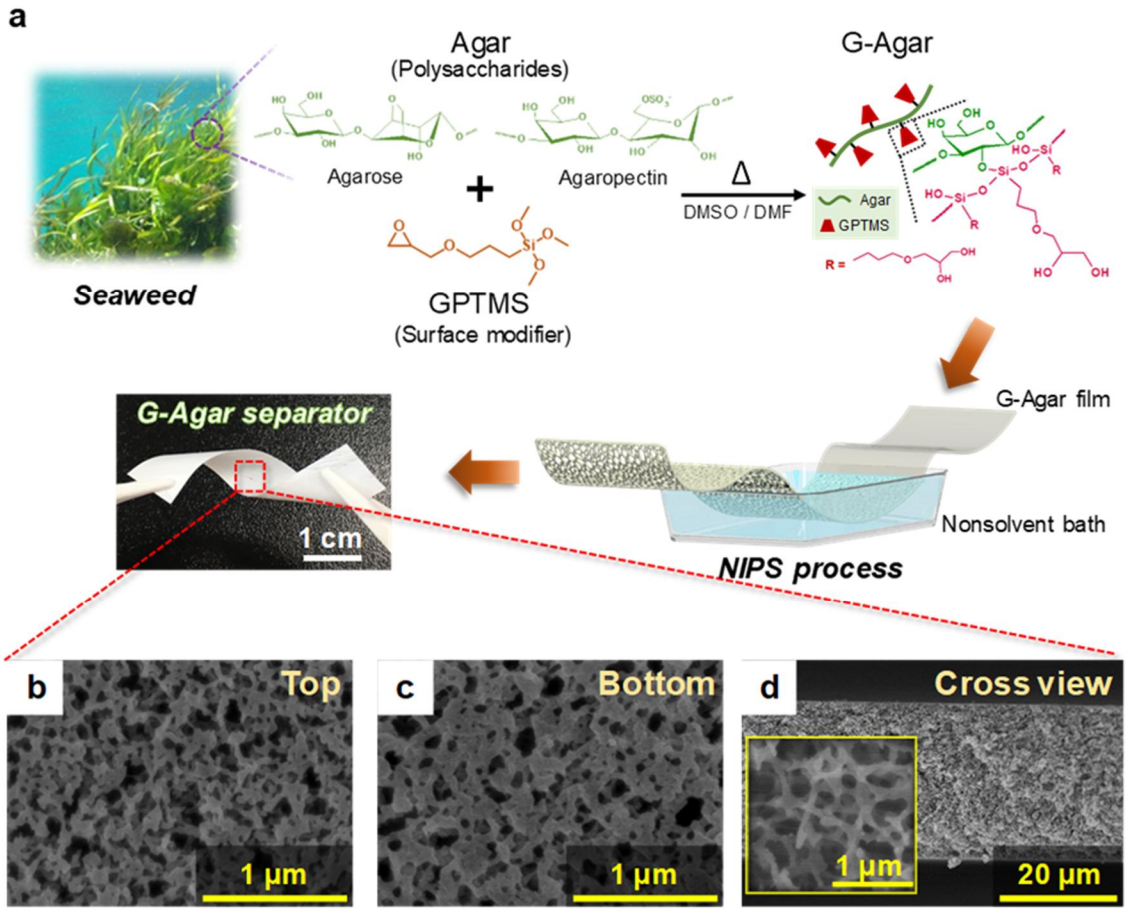

Figure 3-1. Fabrication process and SEM images of G-Agar separator membrane. a) Schematic illustration of the overall fabrication process based on NIPS method. SEM images of G-Agar separator membrane; b) top, c) bottom, and d) cross-sectional views.

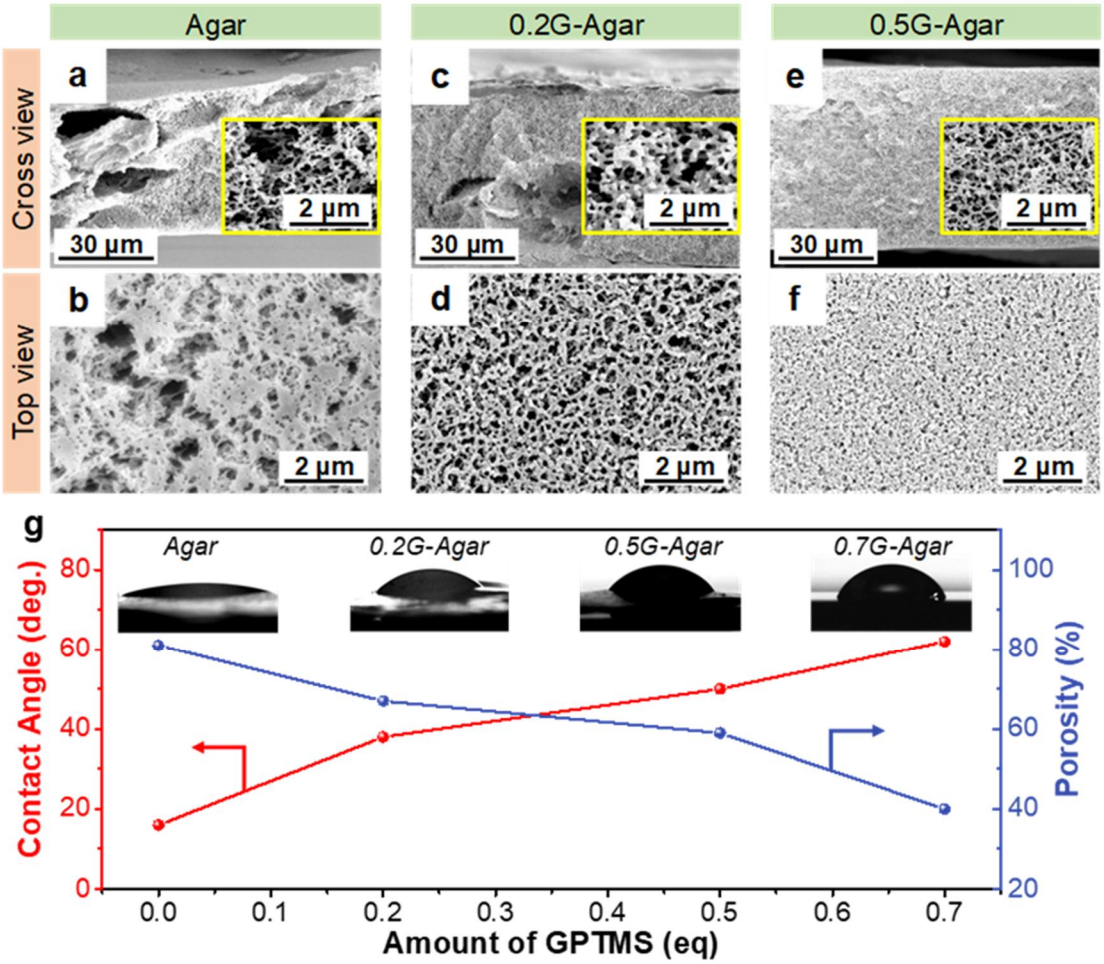

Figure 3-2. Effect of GPTMS content on the porous structure and surface property of the agar separator membrane. SEM images of the agar-based separator membranes a) cross and b) top views: agar separator membrane; c) cross and d) top views: 0.2G-Agar separator membrane; and e) cross and f) top views: 0.5G-Agar separator membrane. The inset shows magnified cross-sectional images. g) Changes in water contact angle and porosity of the agar separator membrane with different GPTMS modifications.

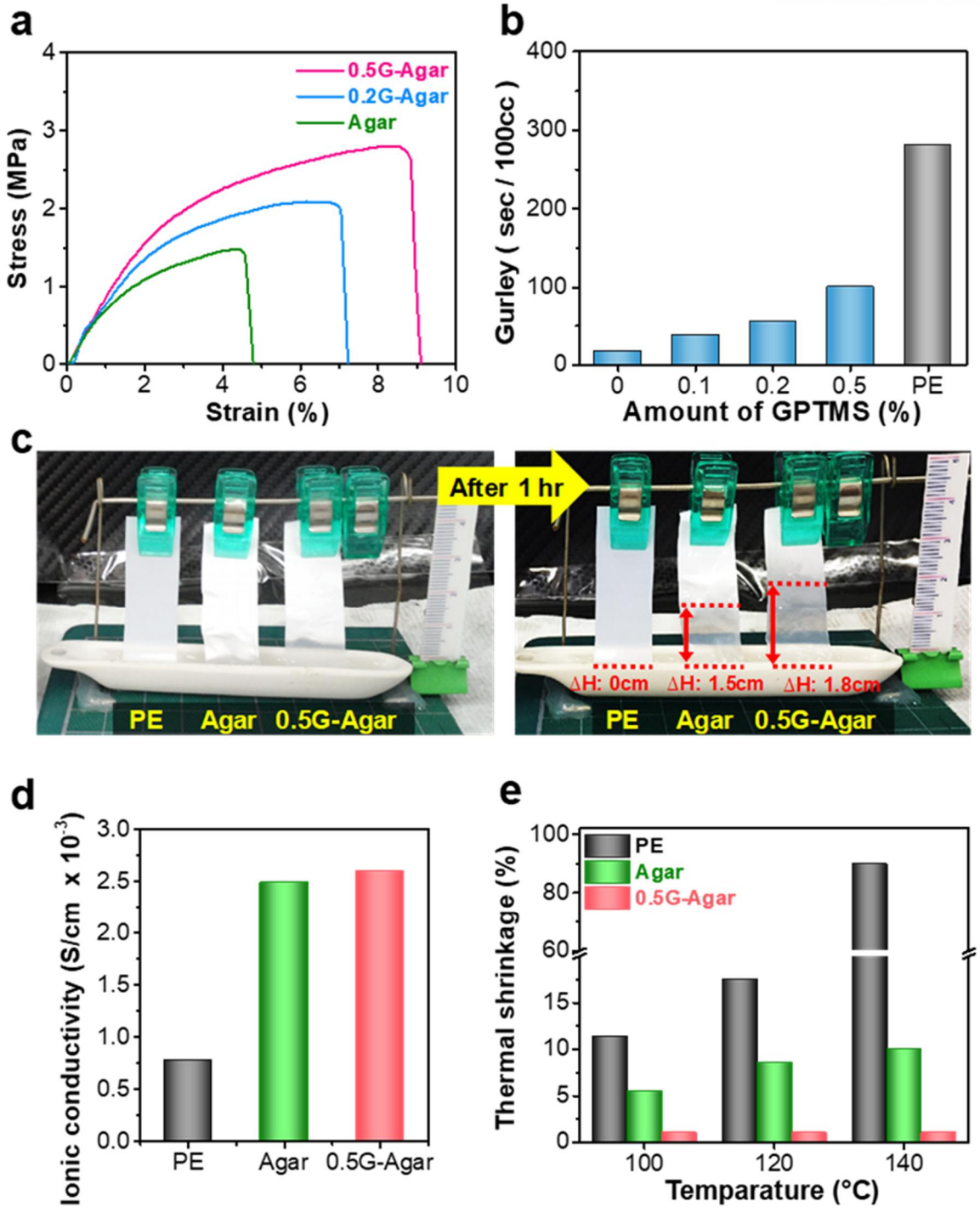

Figure 3-3. Mechanical and physicochemical characterization of PE, agar, and 0.5G-Agar separator membranes. a) Tensile strength, b) changes in Gurley value and porosity, and c) electrolyte wettability test of the agar separator membrane at different GPTMS modifications. d) Ionic conductivity of the PE, agar, and 0.5G-Agar separator membranes. e) Thermal shrinkage of the separator membranes at the different temperature storage for 30 min.

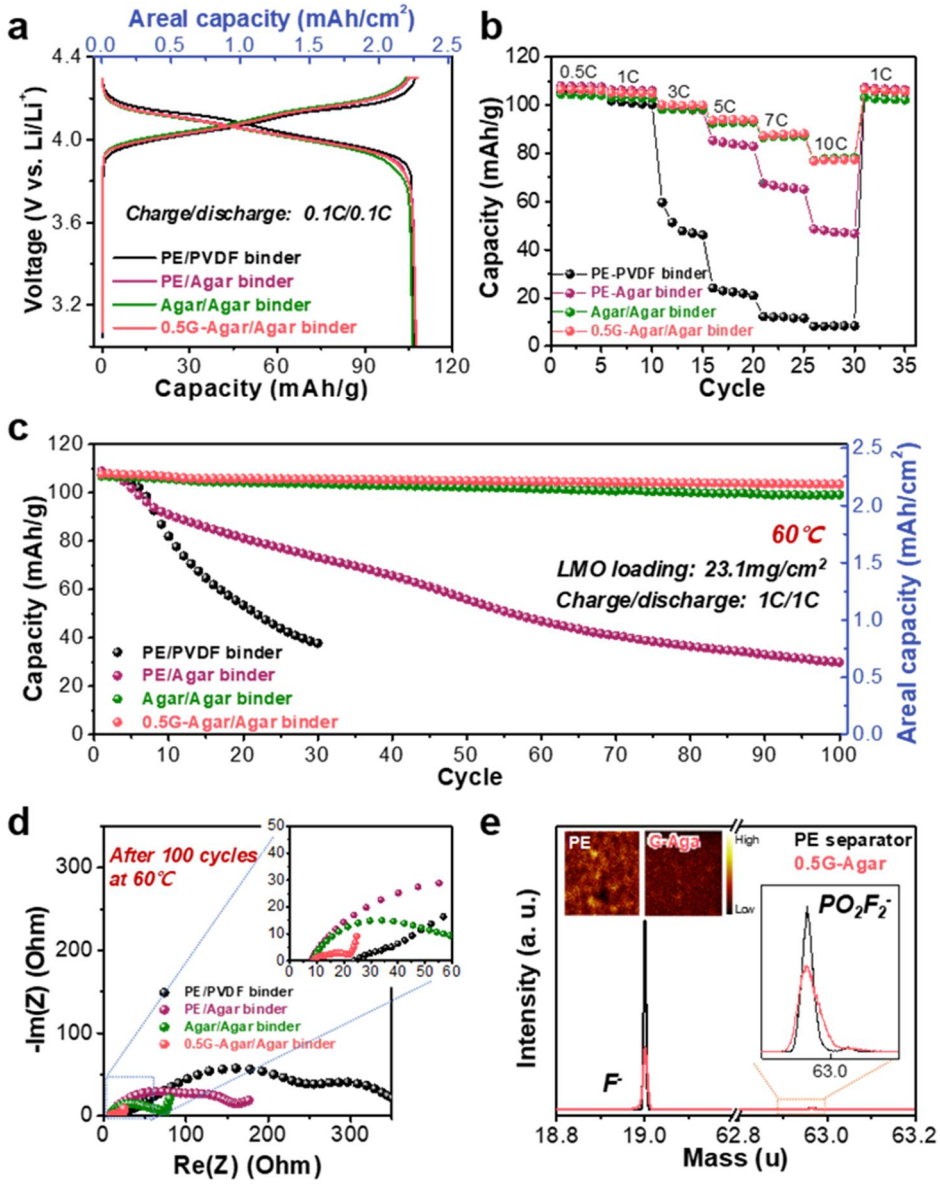

Figure 3-4. Electrochemical performances of an LMO half cell with PE, agar, and 0.5G-Agar separator membranes. a) Galvanostatic charge-discharge curves of the half cell with different separators and binders at a rate of 0.1 C. b) Rate capability of a half cell with each separator/binder over a wide range of discharge current densities (0.5–10.0 C). c) High temperature (60□) cycling performances at a charge–discharge current density (1 C/1 C). d) Nyquist plots (impedance spectra) of the half cell with PE, agar, and 0.5G-Agar separator membranes after 100 cycles at 60□. e) TOF-SIMS analysis of the separator membranes after immersion in a water-contained electrolyte.

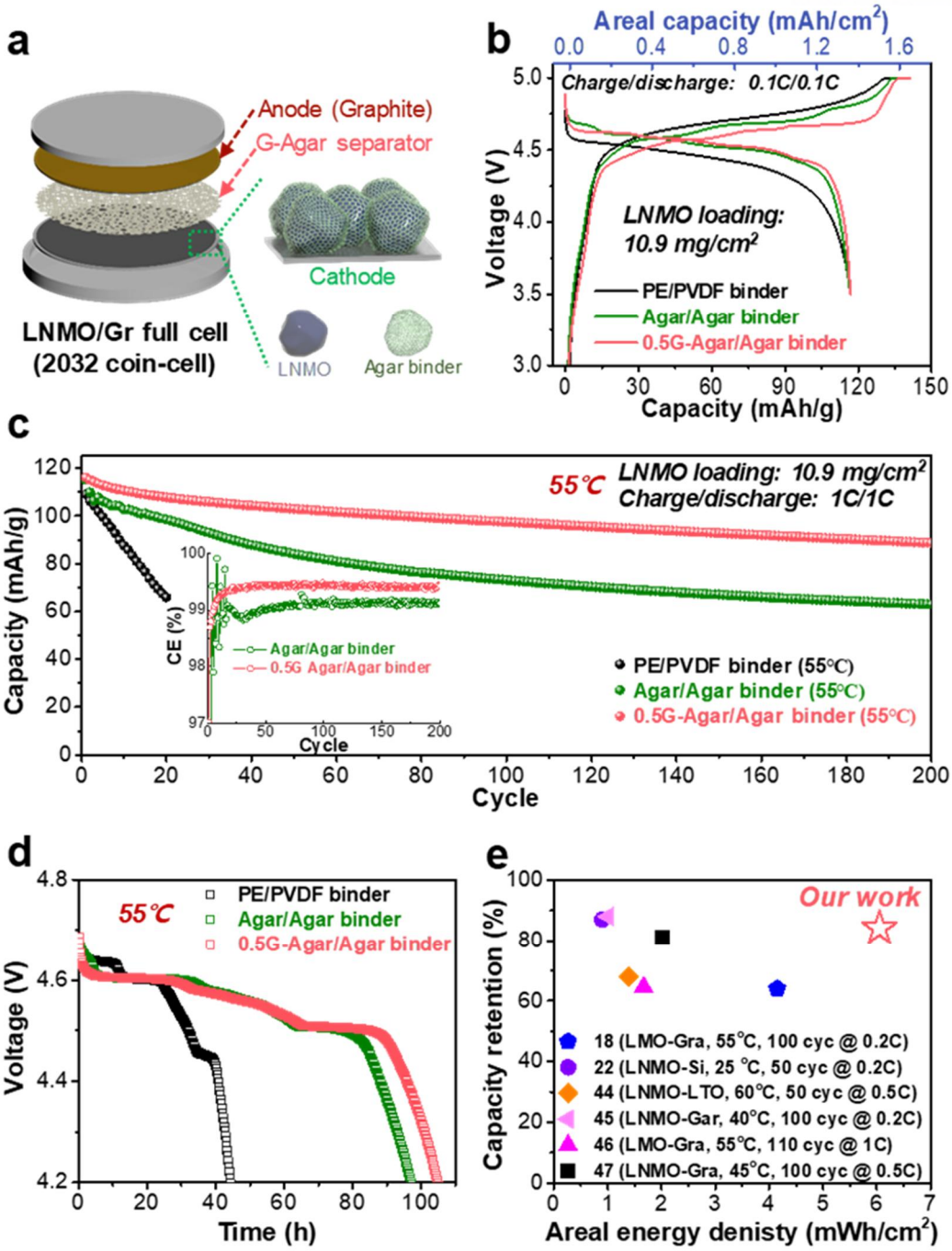

Figure 3-5. Electrochemical performances of LNMO/graphite full cell with PE, agar, and 0.5G-Agar separator membrane. a) Schematic illustration of the LNMO/graphite full cell configuration. b) Galvanostatic charge-discharge curves of full cells with different separators and binder at a rate of 0.1 C. c) Cycling performances at a charge/discharge rate (1 C/1 C) under different temperatures. d) Elevated temperature (55□) storage ability of the full cell with PE, agar, and 0.5G-Agar separator membrane. e) Capacity retention (%) of the LMO or LNMO full cells as a function of areal energy density under high temperature.[18,22,44-47]

Table S3-1. Peak assignment of FT-IR spectra of agar and G-Agar separator

Wavenumber (cm^{-1})	Assignment
1070	C-O-C or Si-O-C
1050	C-O-C in polysaccharides
1015	Si-O-Si

Table S3-2. Fitting results for the impedance spectra in Figure 4e

Samples	$R_{SEI}(\Omega)$	$R_{ct}(\Omega)$
PE/PVDF binder	215	135
PE/Agar binder	127	100
Agar	50	25
0.5G-Agar	7	9

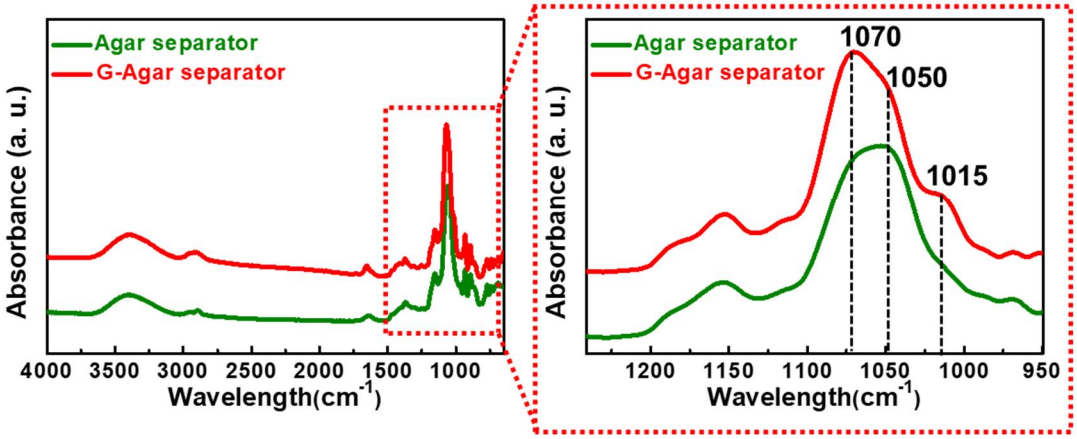

Figure S3-1. FT-IR analysis of agar and G-Agar separator membrane.

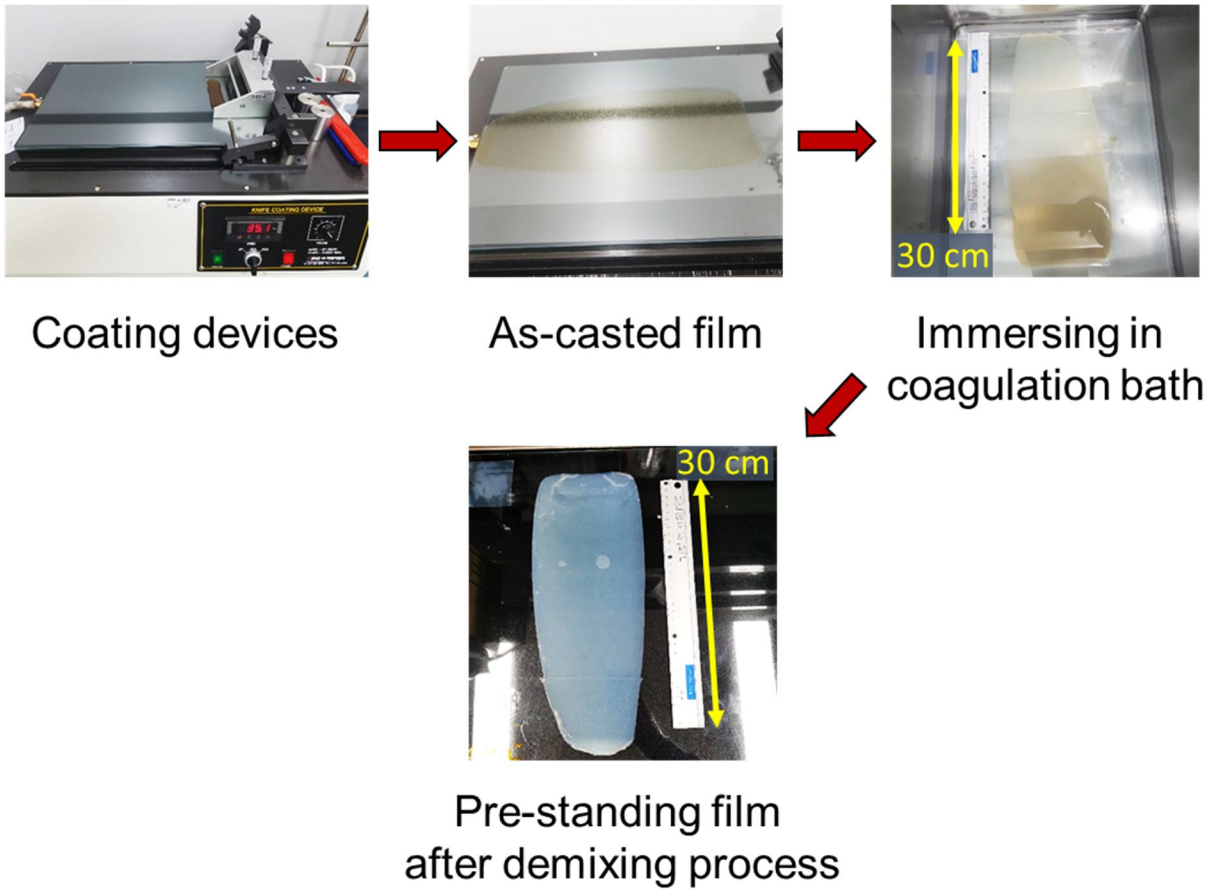

Figure S3-2. Digital photographs of large-scale G-Agar film fabrication process.

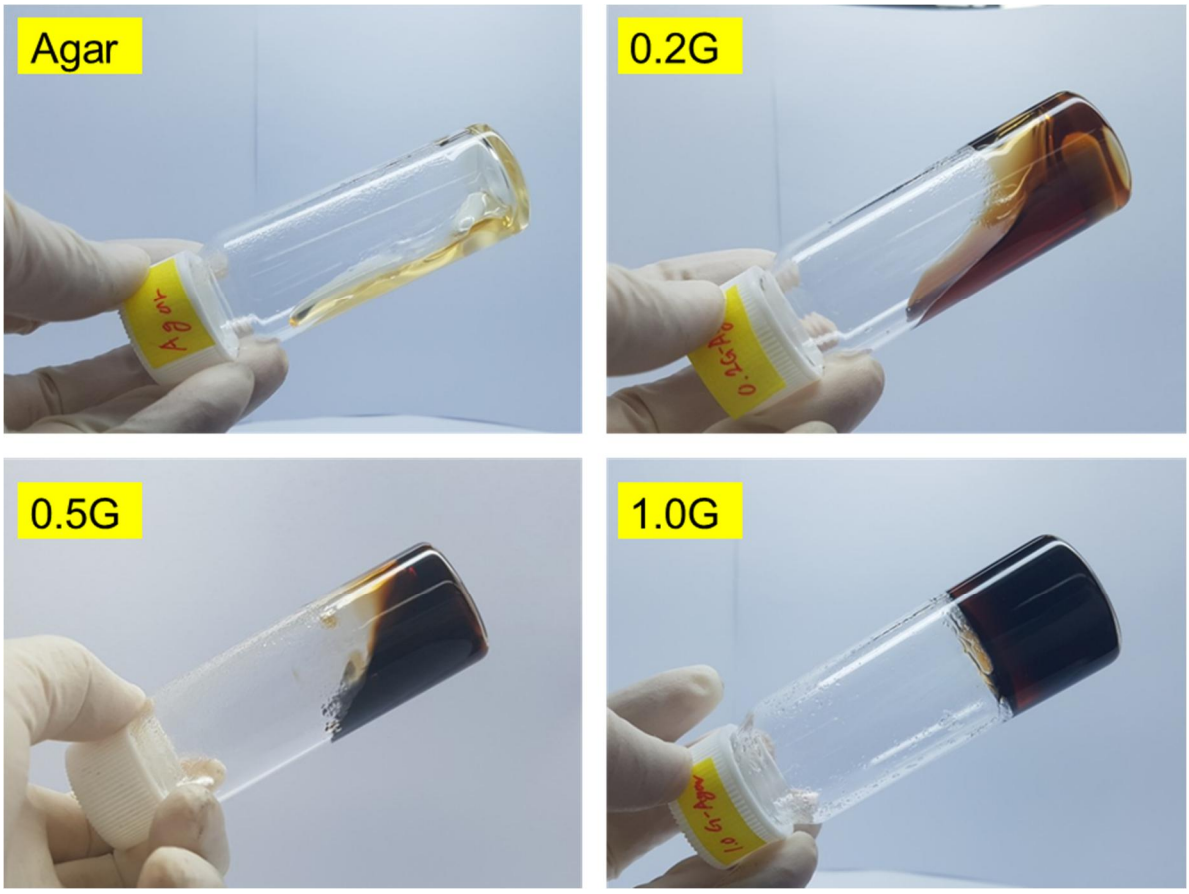

Figure S3-3. Digital photographs of agar and G-Agar solutions with various GPTMS modification.

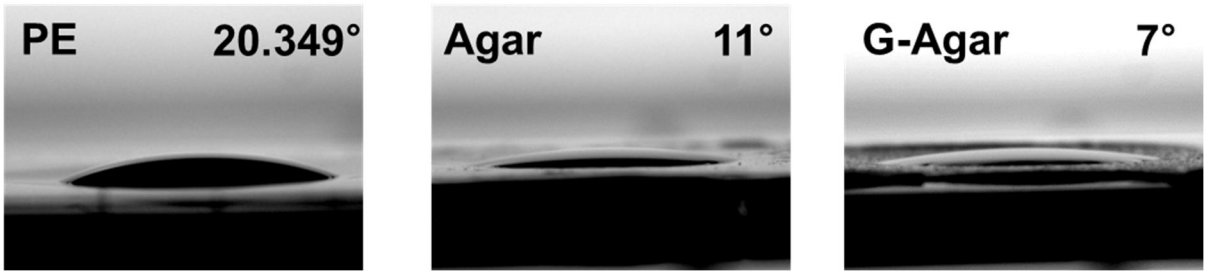

Figure S3-4. Contact angle of agar and G-Agar separator to the electrolyte (1 M $LiPF_6$ in EC/DEC (1/1 v/v)).

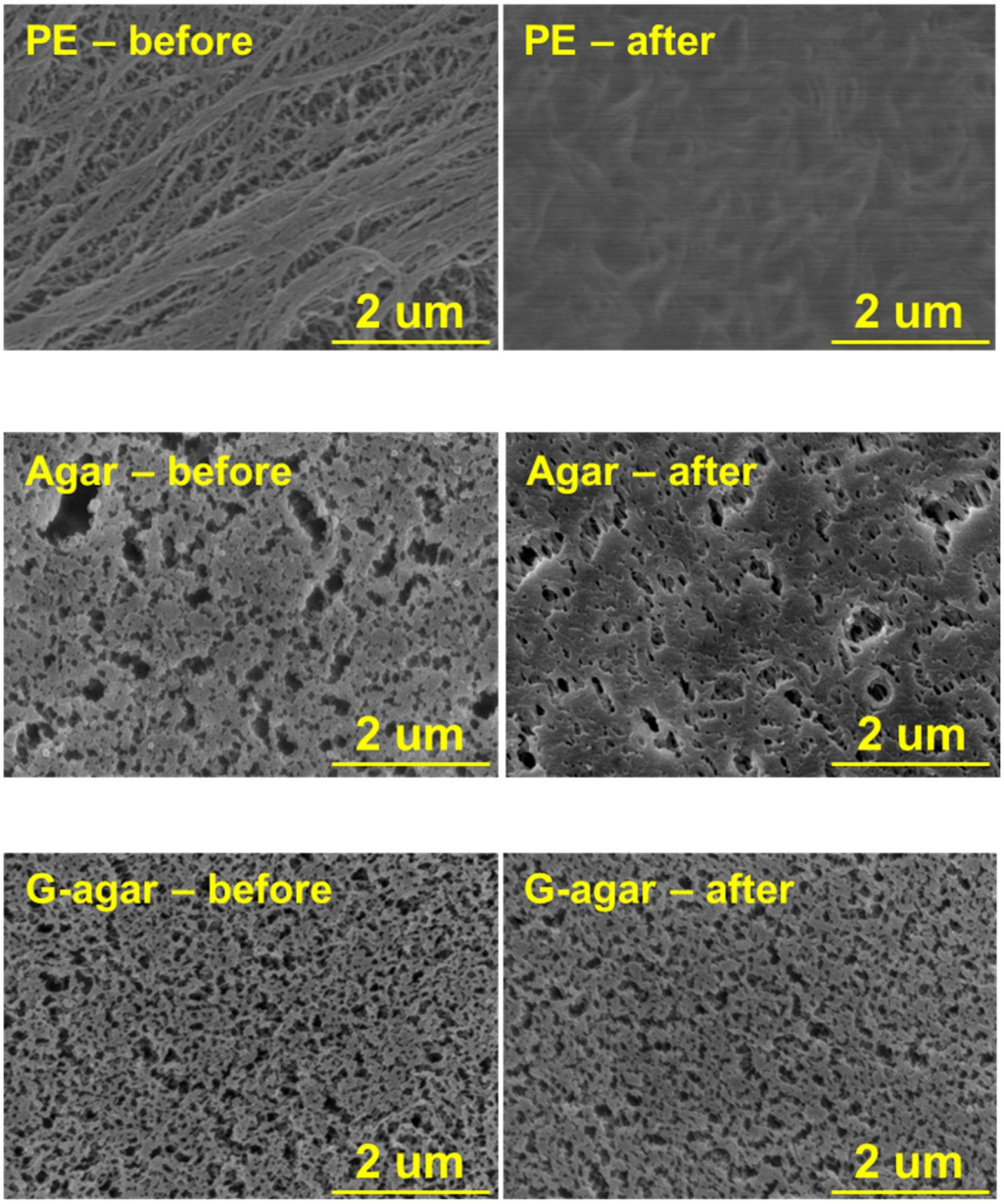

Figure S3-5. SEM images of PE, agar and G-Agar separator before and after thermal treatment.

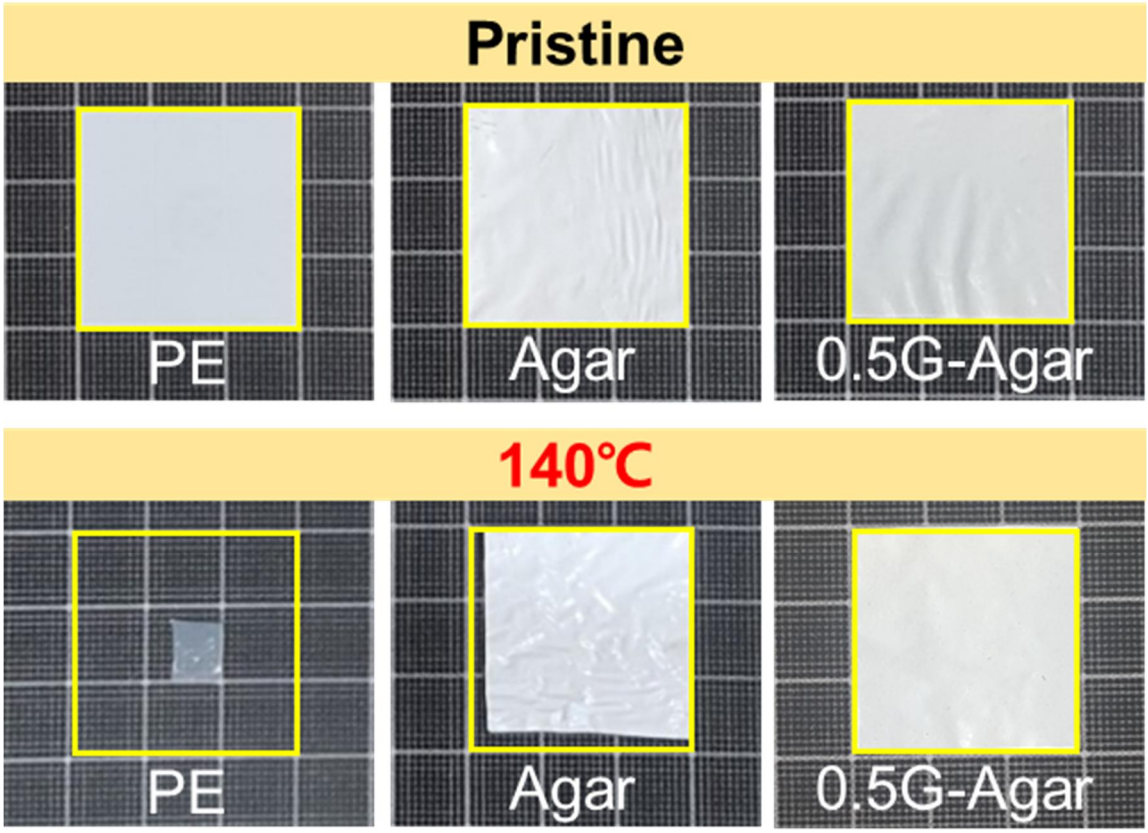

Figure S3-6. Digital photographs of PE, agar and G-Agar separator before and after thermal treatment.

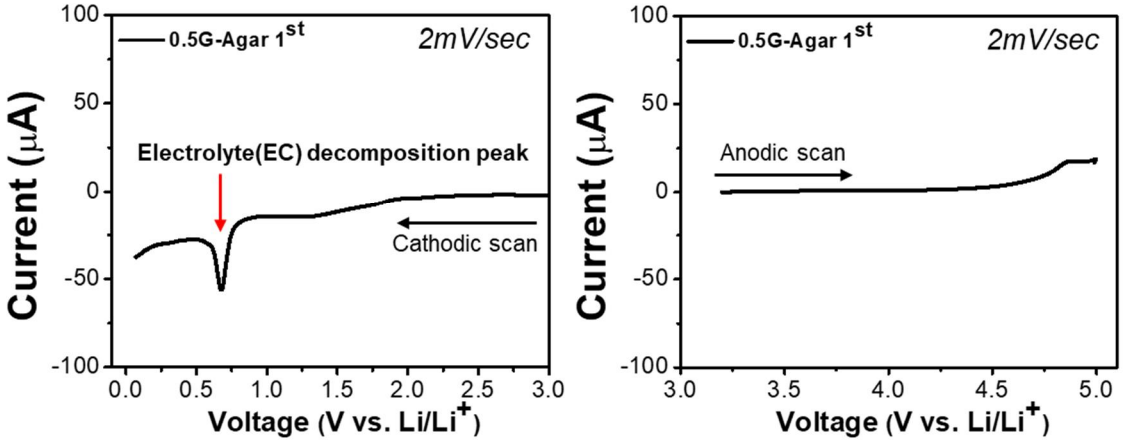

Figure S3-7. Cyclic voltammetry (CV) characterization of 0.5G-Agar separator membrane.

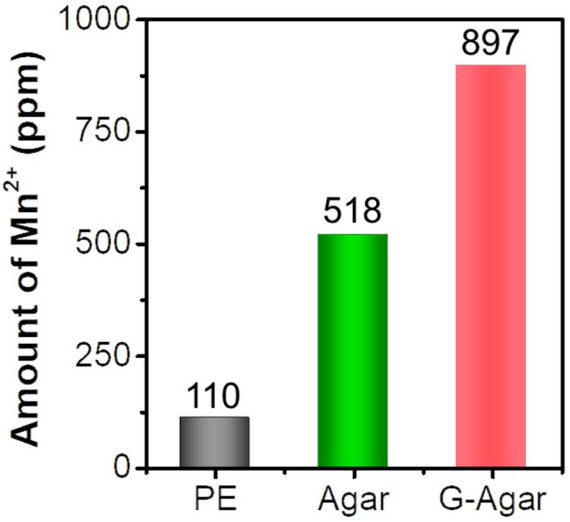

Figure S3-8. ICP-MS results of PE, agar, 0.5G-Agar separator membrane after immersing Mn^{2+} ion contained electrolyte (10mM $Mn(ClO_4)_2$-contained 1M $LiPF_6$ in EC/DEC 1/1 v/v).

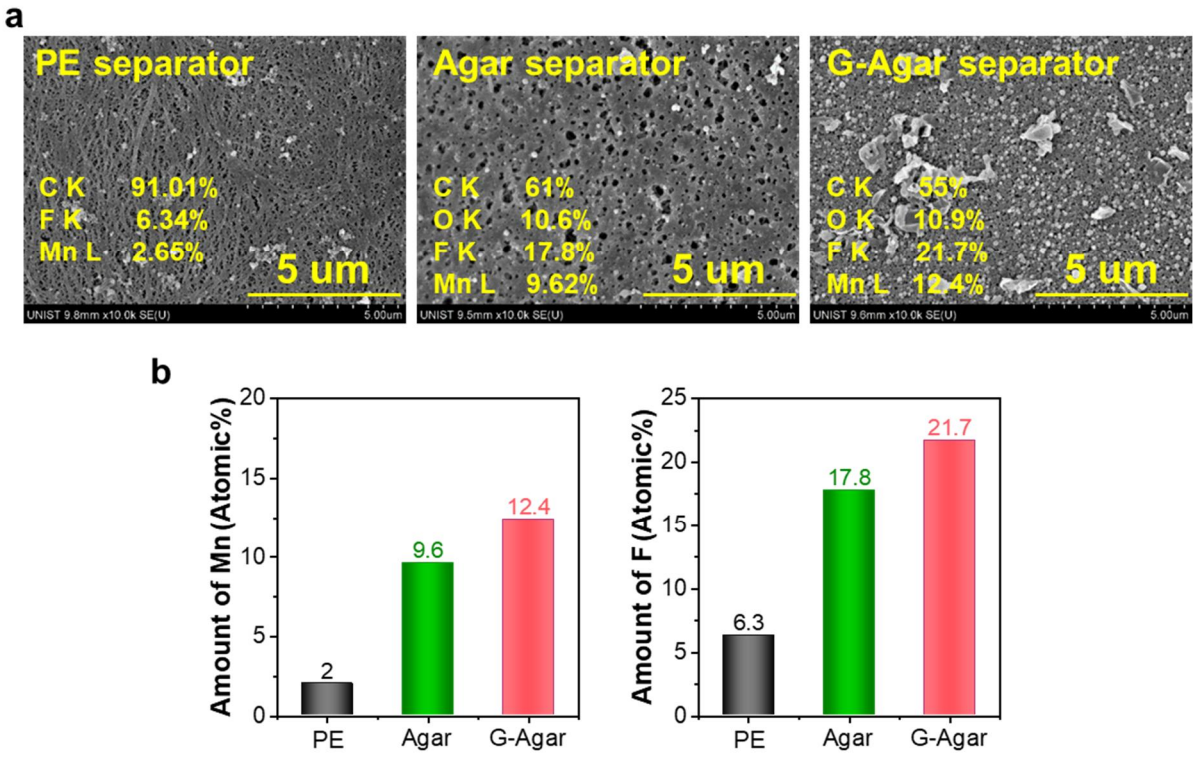

Figure S3-9. a) SEM and b) EDX results of PE, agar, and G-Agar separator after 100 cycles at high temperature.

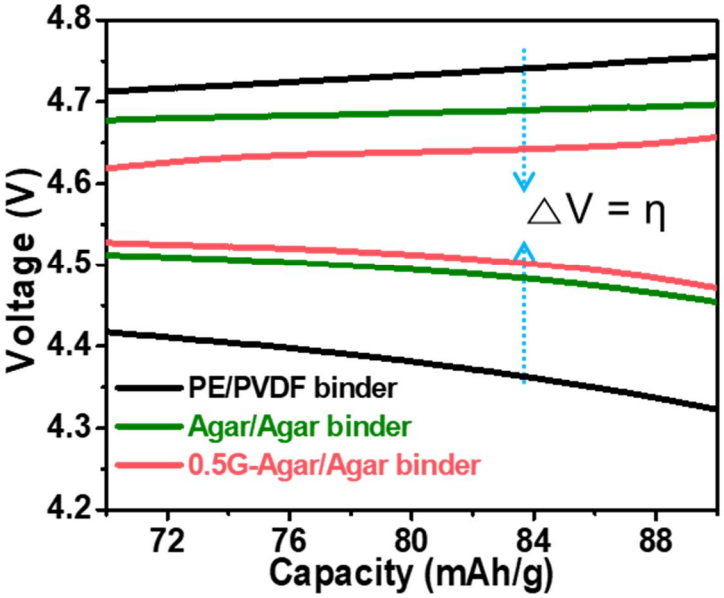

Figure S3-10. Overpotential of PE, agar and G-Agar with LNMO/graphite full cell at first cycle.

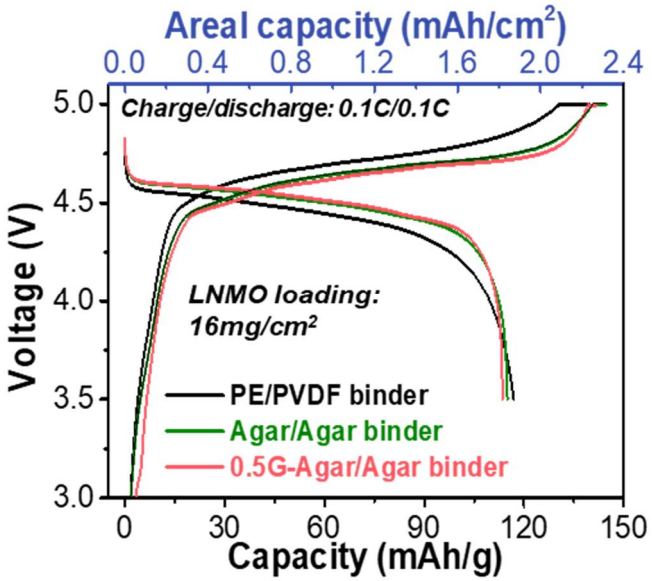

Figure S3-11. Frist cycle of the LNMO/graphite full cell with high loading density (1.9 mA h cm^{-2}) with different separator and binder at a rate of 0.1 C under 25℃.

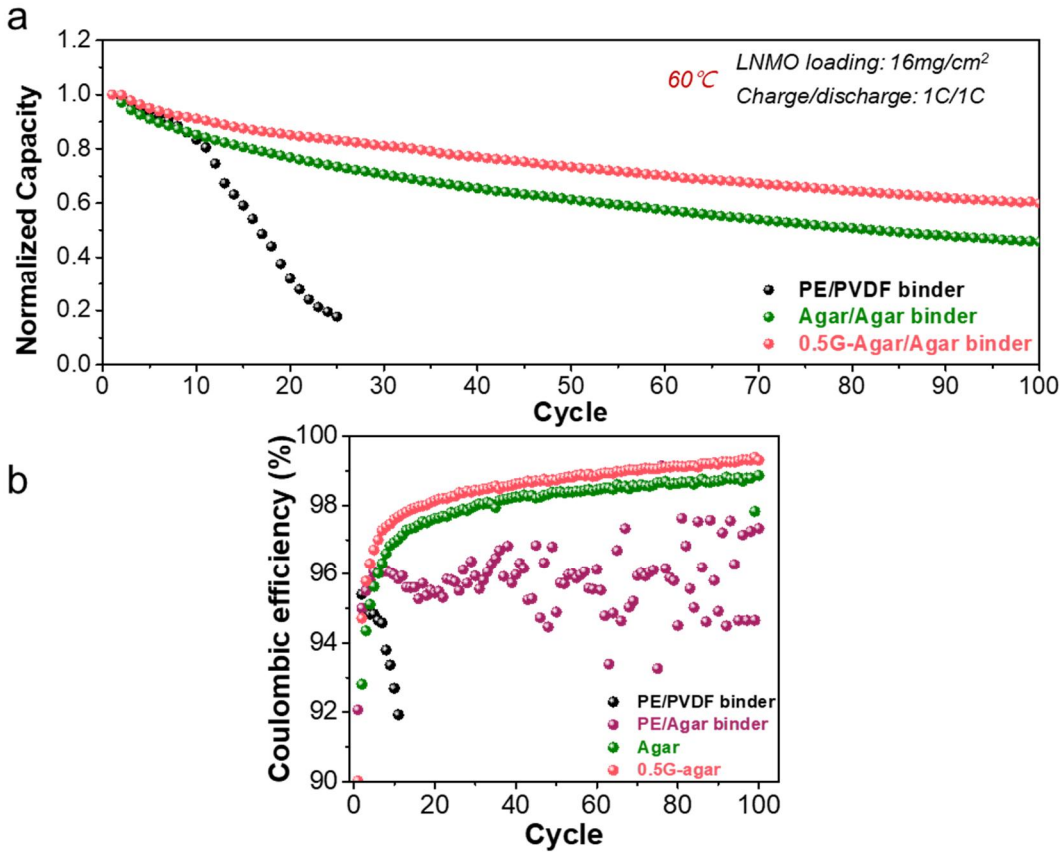

Figure S3-12. a) Cycle performance and b) CE resultof LNMO/graphite full cell with high loading energy density (1.9 mA h cm^{-2}) at a rate of 1 C under 60℃.

3.4 Conclusion

In summary, we demonstrated that agar, which can easily be extracted from seaweeds, could be utilized for the functional binder and separator membrane of LIBs. We fabricated the porous separator membrane by introducing GPTMS as a surface modifier to control the phase separation behavior of agar polymer in the NIPS process. This approach allowed the determination of the final morphologies of membranes for LIBs. By precisely controlling the amount of GPTMS modification, we obtained a highly reliable and practical separator membrane for LIBs with proper porosity, good electrolyte wettability, high ionic conductivity, and superior thermal stability. Moreover, the agar exhibited beneficial abilities such as Mn^{2+} chelation, and PF_5 stabilization. The advantages posed by the G-Agar separator membrane and agar binder make them compatible with high-energy density batteries comprising a Mn-based cathode (LMO half cell and LNMO/graphite full cell), thereby resulting in an outstanding cycle performance (84.1 % after 100 cycles at 55). The multifunctionality and cost-effectiveness of the agar make it feasible for application in a wide range of energy storage devices. Therefore, the proposed agar provides a multifunctional natural material for high-performance batteries.

3.5 Reference

[1] N. Nitta, F. Wu, J. T. Lee, G. Yushin, *Mater. Today.* **2015**, *18*, 252.

[2] M. Armand, J. M. Tarascon, *Nature.* **2001**, *414*, 359.

[3] B. Dunn, H. Kamath, J. Tarascon, *Science.* **2011**, *334*, 928.

[4] W. J. Song, S. H. Joo, D. H. Kim, C. Hwang, G. Y. Jung, S. Bae, Y. Son, J. Cho, H. K. Song, S. K. Kwak, S. Park, S. J. Kang, *Nano Energy.* **2017**, *32*, 255.

[5] John B. Goodenough and Youngsik Kim, *Chem. Mater.* **2010**, *22*, 587.

[6] F. Wu, G. Yushin, *Energy Environ. Sci.* **2017**, *10*, 435.

[7] B. L. Ellis, K. T. Lee, L. F. Nazar, *Chem. Mater.* **2010**, *22*, 691.

[8] G. S. and D. A. Vinodkumar Etacheri, Rotem Marom, Ran Elazari, *Energy Environ. Sci.* **2011**, *4*, 3243.

[9] M. Yoshio, R. J. Brodd and A. Kozawa, *Lithium-Ion Batteries Science and Technologies*, Springer, New York, **2009.**

[10] K. Mizushima, P. C. Jones, P. J. Wiseman and J. B. Goodenough, *Mater. Res. Bull.*, **1980**, *15*, 783.

[11] W. J. Zhang, *J. Power Sources.* **2011**, *196*, 2962.

[12] N. Yabuuchi, T. Ohzuku, *J. Power Sources.* **2003**, *119–121*, 171.

[13] J. M. Tarascon, *J. Electrochem. Soc.* **1991**, *138*, 2859.

[14] Q. Zhong, *J. Electrochem. Soc.* **1997**, *144*, 205.

[15] N. S. Choi, J. G. Han, S. Y. Ha, I. Park, C. K. Back, *RSC Adv.* **2015**, *5*, 2732.

[16] C. Zhan, T. Wu, J. Lu, K. Amine, *Energy Environ. Sci.* **2018**, *11*, 243.

[17] J. Lu, C. Zhan, T. Wu, J. Wen, Y. Lei, A. J. Kropf, H. Wu, D. J. Miller, J. W. Elam, Y. K. Sun, X. Qiu, K. Amine, *Nat. Commun.* **2014**, *5*, 1.

[18] A. Banerjee, B. Ziv, Y. Shilina, S. Luski, I. C. Halalay, D. Aurbach, *Adv. Energy Mater.* **2017**, *7*, 1601556

[19] S. Yoo, J.-H. Kim, M. Shin, H. Park, J.-H. Kim, S.-Y. Lee, S. Park, *Sci. Adv.* **2015**, *1*, e1500101.

[20] R. Zhou, J. Huang, S. Lai, J. Li, F. Wang, Z. Chen, W. Lin, C. Li, J. Wang, J. Zhao, *Sustain. Energy Fuels*. **2018**, *2*, 1481.

[21] J. M. Kim, C. Kim, S. Yoo, J. H. Kim, J. H. Kim, J. M. Lim, S. Park, S. Y. Lee, *J. Mater. Chem. A.* **2015**, *3*, 10687.

[22] G. Hwang, J. M. Kim, D. Hong, C. K. Kim, N. S. Choi, S. Y. Lee, S. Park, *Green Chem.* **2016**, *18*, 2710.

[23] G. O. Phillips and P. A. Williams, *Handbook of Hydrocolloids*, CRC Press, Cleveland, **2000**.

[24] H. P. S. Abdul Khalil, C. K. Saurabh, Y. Y. Tye, T. K. Lai, A. M. Easa, E. Rosamah, M. R. N. Fazita, M. I. Syakir, A. S. Adnan, H. M. Fizree, N. A. S. Aprilia, A. Banerjee, *Renew. Sustain. Energy Rev.* **2017**, *77*, 353.

[25] S. Spirk, *Polysaccharides as Battery Components*, Springer, Switzerland, **2018**.

[26] I. Kovalenko, B. Zdyrko, A. Magasinski, B. Hertzberg, Z. Milicev, R. Burtovyy, I. Luzinov and G. Yushin, *Science*. **2011**, 333, 75.

[27] H. Wu, Y. Cui, *Nano Today.* **2012**, *7*, 414.

[28] M. Murase, N. Yabuuchi, Z. J. Han, J. Y. Son, Y. T. Cui, H. Oji, S. Komaba, *ChemSusChem.* **2012**, *5*, 2307.

[29] E. Callaway, *Nature.* **2015**, *528*, 171.

[30] K. W. Chew, J. C. Juan, S. M. Phang, T. C. Ling, P. L. Show, *Sep. Sci. Technol.* **2018**, *53*, 467.

[31] G. R. Guillen, Y. Pan, M. Li, E. M. V. Hoek, *Ind. Eng. Chem. Res.* **2011**, *50*, 3798.

[32] W. Lu, Z. Yuan, Y. Zhao, H. Zhang, H. Zhang, X. Li, *Chem. Soc. Rev.* **2017**, *46*, 2199.

[33] M. Shin, W.-J. Song, H. B. Son, S. Yoo, S. Kim, G. Song, N.-S. Choi, S. Park, *Adv. Energy Mater.* **2018**, *8*, 1801025.

[34] J. Mulder, *Basic Principles of Membrane Technology*, Kluwer Academic Publishers, London, **2012**.

[35] H. Strathmann, K. Kock, *Desalination.* **1977**, *21*, 241.

[36] H. Lee, M. Yanilmaz, O. Toprakci, K. Fu, X. Zhang, *Energy Environ. Sci.* **2014**, *7*, 3857.

[37] S. S. Zhang, *J. Power Sources.* **2007**, *164*, 351.

[38] P. Arora and Z. Zhang, *Chem. Rev.*, **2004**, *104*, 4419.

[39] C. Man, P. Jiang, K. W. Wong, Y. Zhao, C. Tang, M. Fan, W. M. Lau, J. Mei, S. Li, H. Liu, D. Hui, *J. Mater. Chem. A* **2014**, *2*, 11980.

[40] M. Yang and J. Hou, *Membranes*. **2012**, *2*, 367.

[41] C. Zhan, J. Lu, A. Jeremy Kropf, T. Wu, A. N. Jansen, Y. K. Sun, X. Qiu, K. Amine, *Nat. Commun.* **2013**, *4*, 2437.

[42] S. T. Myung, K. Izumi, S. Komaba, H. Yashiro, H. J. Bang, Y. K. Sun, N. Kumagai, *J. Phys. Chem. C* **2007**, *111*, 4061.

[43] C. K. Kim, D. S. Shin, K. E. Kim, K. Shin, J. J. Woo, S. Kim, S. Y. Hong, N. S. Choi, *ChemElectroChem.* **2016**, *3*, 913.

[44] X. Cao, X. He, J. Wang, H. Liu, S. Röser, B. R. Rad, M. Evertz, B. Streipert, J. Li, R. Wagner, M. Winter, I. Cekic-Laskovic, *ACS Appl. Mater. Interfaces.* **2016**, *8*, 25971.

[45] J. Wang, Y. Yamada, K. Sodeyama, C. H. Chiang, Y. Tateyama, A. Yamada, *Nat. Commun.* **2016**, *7*, 1.

[46] M. H. Ryou, S. Hong, M. Winter, H. Lee, J. W. Choi, *J. Mater. Chem. A* **2013**, *1*, 15224.

[47] P. Hu, Y. Duan, D. Hu, B. Qin, J. Zhang, Q. Wang, Z. Liu, G. Cui, L. Chen, *ACS Appl. Mater. Interfaces* **2015**, *7*, 4720.